nature geoscience

LETTERS

PUBLISHED ONLINE: 9 MAY 2016 | DOI: 10.1038/NGEO2713

Earth's air pressure 2.7 billion years ago constrained to less than half of modern levels

Sanjoy M. Som[1]*†, Roger Buick[1], James W. Hagadorn[2], Tim S. Blake[3], John M. Perreault[1]†, Jelte P. Harnmeijer[1]† and David C. Catling[1]

How the Earth stayed warm several billion years ago when the Sun was considerably fainter is the long-standing problem of the 'faint young Sun paradox'. Because of negligible[1] O_2 and only moderate CO_2 levels[2] in the Archaean atmosphere, methane has been invoked as an auxiliary greenhouse gas[3]. Alternatively, pressure broadening in a thicker atmosphere with a N_2 partial pressure around 1.6–2.4 bar could have enhanced the greenhouse effect[4]. But fossilized raindrop imprints indicate that air pressure 2.7 billion years ago (Gyr) was below twice modern levels and probably below 1.1 bar, precluding such pressure enhancement[5]. This result is supported by nitrogen and argon isotope studies of fluid inclusions in 3.0–3.5 Gyr rocks[6]. Here, we calculate absolute Archaean barometric pressure using the size distribution of gas bubbles in basaltic lava flows that solidified at sea level ∼2.7 Gyr in the Pilbara Craton, Australia. Our data indicate a surprisingly low surface atmospheric pressure of $P_{atm} = 0.23 \pm 0.23$ (2σ) bar, and combined with previous studies suggests ∼0.5 bar as an upper limit to late Archaean P_{atm}. The result implies that the thin atmosphere was rich in auxiliary greenhouse gases and that P_{atm} fluctuated over geologic time to a previously unrecognized extent.

Air pressure constrains atmospheric composition and climate, in turn influencing biological evolution. However, it has proved very difficult to measure atmospheric pressure over geologic time because such a barely perceptible property has minimal impact on most rocks. Nevertheless, Archaean air pressure has been constrained by independent methods[5,6] to ≤1.2 bar. Here, we more tightly constrain ancient air pressure by applying a new proxy to the Archaean eon: the size distribution of gas bubbles (vesicles) in basaltic lava flows erupted at sea level.

The principle involved in using vesicles in basaltic lava flows for palaeobarometry is that the average vesicle size at the very top of a flow is constrained by atmospheric pressure alone, whereas the average vesicle size at the flow base is controlled by the weight of the lava above added to the atmospheric pressure[7]. Thus, the difference in size between large vesicles at the flow top and smaller vesicles at the flow base allows atmospheric pressure to be deduced once basalt density and flow thickness are known. This differential technique is independent of absolute volatile content in the lava, and has been verified as a geologic altimeter on modern flows in Hawaii, where elevations are known[8]. It has also been used to infer the uplift rate of the Colorado plateau[9], yielding results consistent with thermochronology[10], and has been applied to palaeoaltimetry in China[11] and Turkey[12]. However, the technique can be used only on appropriate lava flows, which must be relatively thin, and have cooled from top-down and bottom-up without inflation by injection of new molten material. In such flows, vesiculation mostly accumulates in upper (UVZ) and lower (LVZ) vesicular zones[13]. Furthermore, external gas recharge and deflation by drainage must be precluded. Bubbles trapped in the middle of a lava flow may originate from new lava or gas injection, with inflation generally limited to flows on slopes <2° (ref. 14).

The difference in size between the bubbles trapped in the UVZ and LVZ is related to atmospheric pressure P_{atm} (in Pa) by the combined gas law:

$$\frac{P_{atm} V_{UVZ}}{T_{freeze}} = \frac{(P_{atm} + \rho g H) V_{LVZ}}{T_{freeze}} \Rightarrow P_{atm} = \rho g H (V_r - 1)^{-1} \quad (1)$$

Here ρ is the lava density (typically 2,650 kg m^{-3} for basalt[15]), T_{freeze} the temperature at which the lava solidifies at the flow top and bottom, g the gravitational acceleration (9.8 m s^{-2}), H the thickness of the flow (m), and V_r the ratio V_{UVZ}/V_{LVZ} of the mean volume of UVZ to LVZ bubbles[8].

We examined gas bubbles in subaerial basaltic lava flows from the ∼2.74 Gyr upper Boongal Formation to determine air pressure at that time. These massive pahoehoe flows with billowy scoriaceous flow tops occur in the Pilbara Craton of Western Australia where they are exposed along the Beasley River (Fig. 1). Five conformable subaerial flows (numbered 1–5 in Fig. 2) immediately overlie hyaloclastic breccias capping a thick pile of pillow basalts and hyaloclastites[16]. Two additional localities with similar hyaloclastite–pahoehoe transitions were also investigated (flows 6 and 7 in Fig. 1), one ∼12 km laterally along strike at Moona Well (flow 7) and the other ∼1 km stratigraphically higher in the middle Bunjinah Formation (flow 6). The intrusion of lava toes with cracked glassy rinds from the base of the lowermost basalt flow (Fig. 3a) into underlying hyaloclastic breccia (Fig. 3b) indicates terrestrial emplacement of a pahoehoe lava delta on unconsolidated wet beach gravel. The lateral extent, over 300 km east–west, and thickness, ∼1 km, of the subaqueous basalt pile beneath the beach deposits strongly suggest that the subaerial basalt flows were emplaced beside an ocean at sea level (Supplementary Information). Field observations were used to identify flows that were simply emplaced (minimally inflated or deflated without gas recharge) for

[1]Department of Earth and Space Sciences and Astrobiology Program, University of Washington, Seattle, Washington 98195, USA. [2]Department of Earth Sciences, Denver Museum of Nature & Science, Denver, Colorado 80205, USA. [3]School of Earth and Environment, University of Western Australia, 35 Stirling Highway, Crawley, Western Australia 6009, Australia. †Present addresses: Blue Marble Space Institute of Science, Seattle, Washington 98154, USA, and NASA Ames Research Center, Moffett Field, California 94035, USA (S.M.S.); Department of Geology and Geophysics, University of Alaska—Fairbanks, Alaska 99775, USA (J.M.P.); James Hutton Institute, Invergowrie, Dundee DD2 5DA, UK (J.P.H.). *e-mail: sanjoy@bmsis.org

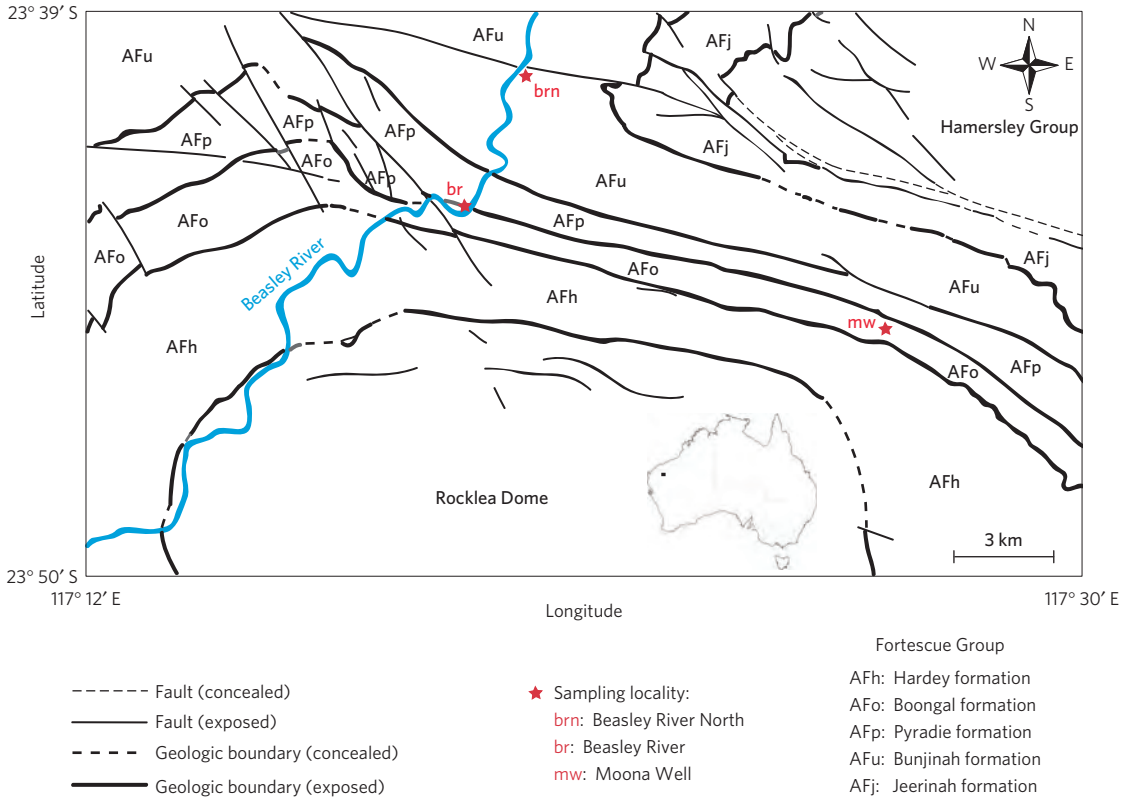

Figure 1 | Geology of the Beasley River field area, southwestern Pilbara, and sampling localities. Flows 1–5 are at the Beasley River site (br), Flow 6 is at the Beasley River North locality (brn), and Flow 7 was at Moona Well (mw).

Figure 2 | Beasley River locality ('br' in Fig. 1) with the locations of five conformable subaerial lava flows, along with the location of collected samples. T, flow top; B, flow bottom. Flow 1 did not have a basal exposure. Geologist (R.B.) in top-left box for scale. (Photos: S. Som.)

subsequent analysis (Supplementary Information). These selection criteria reduced the seven flows studied to only three suitable for analysis: flows 2, 3 and 5 of the Boongal Formation at Beasley River (Fig. 2).

Vesicles in lava flows preserve the original dimensions of the gas bubbles. The rocks underwent pre-compactional alteration during which the vesicles were filled by the secondary minerals quartz, calcite and chlorite to form amygdales[17]. Infilling occurred by passive precipitation without deformation, shown by the absence of expansion or contraction cracks around the amygdales[17] in thin section (Fig. 3c) and by their spherical shape in all but the uppermost flow crusts, where they are ellipsoidal owing to viscous stretching in the solidifying lava. Later low-grade metamorphism (sub-greenschist to lowermost greenschist facies) transformed the basalt matrix to a chlorite–albite–epidote–actinolite assemblage with little concomitant deformation; in the field the rocks are unfoliated and only openly folded with dips of less than 50°. These post-depositional effects altered neither the thickness of the flows nor the size of the amygdales, shown by spherical rather than oblate or prolate shape of the amygdales.

Cores were drilled in samples collected from each UVZ and LVZ for subsequent X-ray analyses. Amygdales were identified by density contrast in the X-ray slices of the cores using a dynamic thresholding algorithm[17]. Tomography software BLOB3D[18] stacked the resulting binary images to determine amygdale dimensions. Mean amygdale volumes and their uncertainties were obtained by bootstrap statistical resampling coupled with the Central Limit Theorem (CLT) (Methods and Supplementary Information). The CLT states that the means of samples taken randomly from a population will be normally distributed, and the mean of this distribution will be the mean of the population. The standard deviation in the bootstrap sampling distribution of the mean gave error bars for the amygdale volumes in the UVZ and LVZ.

In an uninflated flow of thickness H, the vesicle size difference across the flow records atmospheric pressure. From equation (1), the uncertainty in pressure results from combining the uncertainties in the vesicle volumes in the UVZ and LVZ, the flow thickness, and lava density (Supplementary Information). Results are shown in Table 1. The average pressure calculated from the three suitable flows suggests that the sea-level air pressure at 2.74 Gyr was 0.23 ± 0.23 bar (2σ error—see Methods). The 'most probable' air-pressure upper limit obtained from nearly contemporaneous 2.73 Gyr fossil raindrop impressions[5] was 0.52–1.1 bar, whereas isotopic studies[6] on 3.0–3.5 Gyr rocks suggest an upper limit of 0.5–1.2 bar. By combining these previous results with this study, we obtain a more stringent upper limit on the air pressure at ~2.7 Gyr of ~0.5 bar.

A balance of N source and sink fluxes that differs from the modern balance is needed to explain an unusually low Archaean air pressure (much less than obtained by subtracting 0.2 bar of the current O_2 level). At present, a N source flux of 0.33 ± 0.08 Tmol N yr^{-1} (composed of 0.15 ± 0.03 Tmol N yr^{-1}

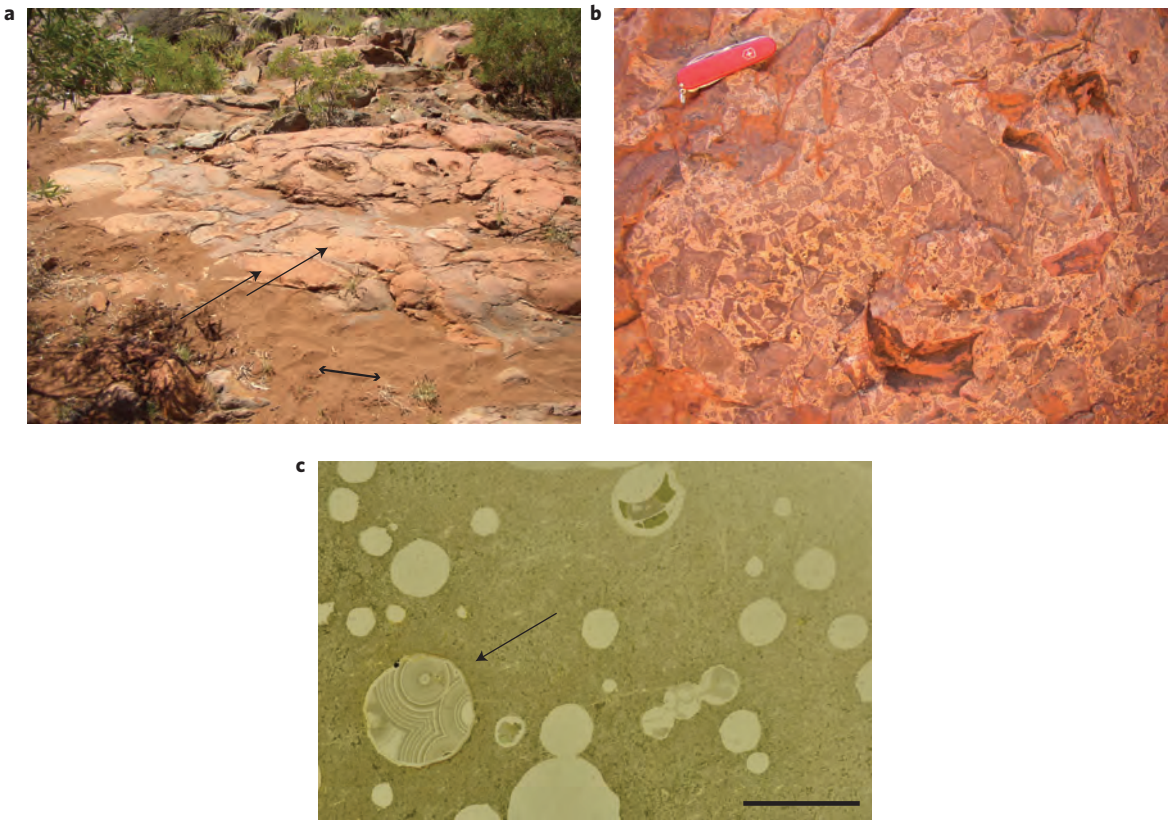

Figure 3 | Beasley River geologic context and flow detail. a, The intrusion of brown lava toes (arrowed) with cracked glassy rinds from the base of the lowermost basalt flow into underlying grey hyaloclastic breccia at the Beasley River site—30 cm modern human footprint in sand for scale (double arrow). **b**, Underlying hyaloclastic breccia with 8.3-cm-long pocket knife for scale. (Photos: S. Som). **c**, Transmitted-light photograph of an amygdale-rich Boongal basalt (top of Flow 2). Arrow shows a large amygdale with concentric filling; scale bar, 1 cm. Note the circular shape of the amygdales and lack of cracks, showing that secondary mineral infilling did not alter the shape of the original vesicles. (Photos: T. Tobin, adapted from ref. 17.)

Table 1 | Results of amygdale size distribution from X-ray computed tomography.

Flow number	Thickness (m)	No. of vesicles top (bottom)	r_t (mm)	V_t (mm^3)	σV_t (mm^3)	r_b (mm)	V_b (mm^3)	σV_b (mm^3)	P_{atm} (bar)	$2\sigma P_{atm}$ (bar)
2	2.24	885 (429)	0.81	2.25	0.14	0.47	0.43	0.03	0.14	0.04
3	1.52	328 (236)	0.88	2.83	0.29	0.53	0.62	0.08	0.11	0.05
5	0.93	627 (631)	0.61	0.97	0.09	0.53	0.61	0.04	0.40	0.23

Measured atmospheric pressures are according to equation (1). The various symbols in the table columns are as follows: r_t = mean amygdale radius at flow top; V_t = mean amygdale volume of top flow as determined by the bootstrap and CLT; σV_t = standard error in amygdale volume at flow top determined by the bootstrap and CLT; r_b = mean amygdale radius at flow bottom; V_b = mean amygdale volume of bottom flow as determined by the bootstrap and CLT; σV_b = standard error in amygdale volume at flow bottom determined by the bootstrap and CLT; P_{atm} = sea-level atmospheric pressure; $2\sigma P_{atm} = 2 \times$ standard error in P_{atm}.

weathering of organic nitrogen plus 0.18 ± 0.07 Tmol N yr^{-1} outgassing) is balanced by loss of N to organic burial[19] of 0.4 ± 0.2 Tmol N yr^{-1}, which includes a minor input flux into subduction zones of 0.094 ± 0.015 Tmol N yr^{-1} today[20] (Supplementary Information). Modern geologic N fluxes imply that a lack of oxidative weathering before the Great Oxidation Event (GOE) at ~2.4–2.3 Gyr would remove about half of the N source flux to the atmosphere. So, a lower Archaean nitrogen partial pressure (pN_2) is consistent with a smaller, pre-GOE nitrogen source flux.

The subduction sink flux of N was also potentially greater in the Archaean than today. If N was not in the atmosphere, it must have been inside the solid Earth. The current amount of N_2 in the mantle and crust[4] is estimated as $\sim 2.1 \pm 1$ bar, with only 0.8 bar of N_2 in the air. At 4.5–4.4 Gyr ago, most mantle nitrogen probably degassed after the Moon-forming impact[21]. Abiotic nitrogen fixation fluxes by lightning[22] and HCN formation and deposition[23] are less than 0.021 Tmol N yr^{-1} each[24]. These could sequester only ~0.2 bar of N_2 over the 1.8 Gyr from Earth's accretion to Boongal deposition. However, ammonification following biological nitrogen fixation was present by 3.2 Gyr (ref. 25), or even 3.8 Gyr (ref. 26), which should have sustained ammonium as the dominant form of nitrogen in the anoxic deep ocean rather than nitrate as today[27]. Thus, a hypothesis for sequestration of N into the solid Earth emerges given that, in anoxic seawater, aqueous ammonium (NH_4^+) will substitute for K^+ in phyllosilicate minerals. Following diagenesis and metamorphism, refractory ammoniated silicates remained in the crust or were subducted, thus burying formerly atmospheric nitrogen. High NH_4^+ levels in 3.8 Gyr metasediments where the original source minerals were clays[26,28] support this hypothesis.

Following the onset of oxidative weathering after the GOE, nitrogen must have returned to the atmosphere through biological denitrification, although an alternative possibility is that oxidized sediments that were subducted could have changed the speciation of

nitrogen in the mantle wedge[29] from NH_4^+ to N_2, allowing a greater N_2 flux from volcanic arcs. With the modern ~0.33 Tmol N yr^{-1} released by volcanoes and weathering, 0.3 bar of N_2 would be replenished in ~0.33 Gyr (Supplementary Information).

Low Archaean air pressure makes it difficult to reconcile the 'faint young Sun' with the geologic record by invoking enhanced atmospheric infrared absorption[4] caused by high pN_2. Rather, greenhouse gases such as methane must have augmented the greenhouse effect provided by moderate levels of CO_2. If the mean P_{atm} (0.23 bar) indicated by our data represents the actual atmospheric pressure during the late Archaean, the corresponding boiling point of water at ~58 °C would be an upper bound to ambient temperature. Furthermore, results from photochemical models of the Archaean atmosphere, such as those that explain the record of mass-independent isotopic fractionation of sulfur, might need to be re-evaluated, because air pressure affects penetration of ultraviolet light and pressure-dependent photochemical reactions. Finally, the 0.5 bar upper limit to Archaean air pressure indicated by our results implies that P_{atm} has fluctuated over time to a greater extent than previously recognized, and that standard temperature and pressure (STP) cannot be presumed for Archaean chemical reactions.

Methods

Methods and any associated references are available in the online version of the paper.

Received 8 March 2016; accepted 13 April 2016; published online 9 May 2016

References

1. Holland, H. D. The oxygenation of the atmosphere and oceans. *Phil. Trans. R. Soc. B* **361,** 903–915 (2006).
2. Sheldon, N. D. Precambrian paleosols and atmospheric CO_2 levels. *Precambr. Res.* **147,** 148–155 (2006).
3. Kasting, J. F. & Siefert, J. L. Life and the evolution of Earth's atmosphere. *Science* **296,** 1066–1068 (2002).
4. Goldblatt, C. *et al*. Nitrogen-enhanced greenhouse warming on early Earth. *Nature Geosci.* **2,** 891–896 (2009).
5. Som, S. M., Catling, D. C., Harnmeijer, J. P., Polivka, P. M. & Buick, R. Air density 2.7 billion years ago limited to less than twice modern levels by fossil raindrop imprints. *Nature* **484,** 359–362 (2012).
6. Marty, B., Zimmermann, L., Pujol, M., Burgess, R. & Philippot, P. Nitrogen isotopic composition and density of the Archean atmosphere. *Science* **342,** 101–104 (2013).
7. Sahagian, D. L. & Maus, J. E. Basalt vesicularity as a measure of atmospheric pressure and palaeoelevation. *Nature* **372,** 449–451 (1994).
8. Sahagian, D., Proussevitch, A. & Carlson, W. Analysis of vesicular basalts and lava emplacement processes for application as a paleobarometer/paleoaltimeter. *J. Geol.* **110,** 671–685 (2002).
9. Sahagian, D., Proussevitch, A. & Carlson, W. Timing of Colorado Plateau uplift: initial constraints from vesicular basalt-derived paleoelevations. *Geology* **30,** 807–810 (2002).
10. Flowers, R. & Farley, K. Apatite $^4He/^3He$ and (U-Th)/He evidence for an ancient Grand Canyon. *Science* **338,** 1616–1619 (2012).
11. Xia, G. Q., Yi, H. S., Zhao, X. X., Gong, D. X. & Ji, C. J. A late Mesozoic high plateau in eastern China: evidence from basalt vesicular paleoaltimetry. *Chin. Sci. Bull.* **57,** 2767–2777 (2012).
12. Aydar, E. *et al*. Central Anatolian Plateau, Turkey: incision and paleoaltimetry recorded from volcanic rocks. *Turk. J. Earth Sci.* **22,** 739–746 (2013).
13. Aubele, J. C., Crumpler, L. & Elston, W. E. Vesicle zonation and vertical structure of basalt flows. *J. Volcanol. Geotherm. Res.* **35,** 349–374 (1988).
14. Hon, K., Kauahikaua, J., Denlinger, R. & Mackay, K. Emplacement and inflation of pahoehoe sheet flows: observations and measurements of active lava flows on Kilauea Volcano, Hawaii. *Geol. Soc. Am. Bull.* **106,** 351–370 (1994).
15. Moore, J. G. Density of basalt core from Hilo drill hole, Hawaii. *J. Volcanol. Geotherm. Res.* **112,** 221–230 (2001).
16. Blake, T. S. Late Archaean crustal extension, sedimentary basin formation, flood basalt volcanism and continental rifting: the Nullagine and Mount Jope Supersequences, Western Australia. *Precambr. Res.* **60,** 185–241 (1993).
17. Som, S. M. *et al*. Quantitative discrimination between geological materials with variable density contrast by high resolution X-ray computed tomography: an example using amygdule size-distribution in ancient lava flows. *Comput. Geosci.* **54,** 231–238 (2013).
18. Ketcham, R. A. Computational methods for quantitative analysis of three-dimensional features in geological specimens. *Geosphere* **1,** 32–41 (2005).
19. Berner, R. Geological nitrogen cycle and atmospheric N_2 over Phanerozoic time. *Geology* **34,** 413–415 (2006).
20. Busigny, V., Cartigny, P. & Philippot, P. Nitrogen isotopes in ophiolitic metagabbros: a re-evaluation of modern nitrogen fluxes in subduction zones and implication for the early Earth atmosphere. *Geochim. Cosmochim. Acta* **75,** 7502–7521 (2011).
21. Turner, G. The outgassing history of the Earth's atmosphere. *J. Geol. Soc. Lond.* **146,** 147–154 (1989).
22. Navarro-González, R., McKay, C. P. & Mvondo, D. N. A possible nitrogen crisis for Archaean life due to reduced nitrogen fixation by lightning. *Nature* **412,** 61–64 (2001).
23. Zahnle, K. J. Photochemistry of methane and the formation of hydrocyanic acid (HCN) in the Earth's early atmosphere. *J. Geophys. Res.* **91,** 2819–2834 (1986).
24. Kasting, J. F. & Siefert, J. L. The nitrogen fix. *Nature* **412,** 26–27 (2001).
25. Stüeken, E., Buick, R., Guy, B. & Koehler, M. C. Isotopic evidence for biological nitrogen fixation by molybdenum-nitrogenase from 3.2 Gyr. *Nature* **520,** 666–669 (2015).
26. Papineau, D., Mojzsis, S., Karhu, J. & Marty, B. Nitrogen isotopic composition of ammoniated phyllosilicates: case studies from Precambrian metamorphosed sedimentary rocks. *Chem. Geol.* **216,** 37–58 (2005).
27. Holland, H. Volcanic gases, black smokers, and the Great Oxidation Event. *Geochim. Cosmochim. Acta* **66,** 3811–3826 (2002).
28. Honma, H. High ammonium contents in the 3800 Ma Isua supracrustal rocks, central West Greenland. *Geochim. Cosmochim. Acta* **60,** 2173–2178 (1996).
29. Mikhail, S. & Sverjensky, D. A. Nitrogen speciation in upper mantle fluids and the origin of Earth's nitrogen-rich atmosphere. *Nature Geosci.* **7,** 2–5 (2014).

Acknowledgements

This work was supported by NASA Exobiology/Astrobiology grant NNX08AP56G to R.B. Additional support came from NASA Astrobiology Institute grant NNA13AA93A. The Washington State University Geoanalytical Laboratory performed the major- and trace-element analyses. S.M.S. thanks E. Stüeken for insightful conversations on K^+ replacement in clays. We thank S. Mikhail, D. Sahagian and B. Marty for helpful reviews.

Author contributions

R.B. conceived the project and led the field work in Western Australia, T.S.B. discovered the locality, J.P.H. assisted in mapping the locality, D.C.C. supervised the data analysis and contributed to the geologic N cycle interpretation, J.W.H. supervised the X-ray work, J.M.P. assisted in extracting amygdale dimensions, S.M.S. assisted in the Beasley River field work, prepared samples for analysis, X-rayed the cores, developed the algorithm to analyse the X-ray images, led the amygdale dimension extraction task, analysed the data, and contributed to the geologic N cycle interpretation. S.M.S., R.B. and D.C.C. wrote the manuscript.

Additional information

Supplementary information is available in the online version of the paper. Reprints and permissions information is available online at www.nature.com/reprints. Correspondence and requests for materials should be addressed to S.M.S.

Competing financial interests

The authors declare no competing financial interests.

Methods

Cores 2.5 cm in diameter were drilled 5 cm into the UVZ and LVZ from each flow's margin (avoiding flow crusts) to provide sub-samples of consistent size and shape for X-ray analysis to determine amygdale dimensions. Eighty-five cores were scanned using a Skyscan 1172 X-ray micro-tomograph at 100 kV and 100 μA, with a resolution of 0.03 mm. 800–1,300 X-ray slices were generated per core and a dynamic thresholding algorithm[17] was used to identify amygdale locations in the X-ray images. The tomography software BLOB3D[18] was then used to stack the resulting binary images and extract amygdale dimensions.

To obtain the mean amygdale volumes and their uncertainties, bootstrap resampling was coupled with the Central Limit Theorem (CLT)[17]. Defining each data set as all the amygdales extracted from a flow's UVZ or LVZ, the bootstrap method creates new data sets (2000 in this case) by randomly sampling with replacement from the original data set. The CLT states that the means of samples taken randomly from a population will be normally distributed and the mean of this distribution will be the mean of the population[30]. Thus, the mean and its error bar from the bootstrap sampling distribution of means provides the average amygdale volume and its uncertainty in the UVZ and LVZ (Supplementary Information).

Only three thin flows were identified in the field as uninflated, undeflated, and showing no evidence of external gas charge. The average pressure calculated from these three flows suggests that the sea-level air pressure at 2.74 Gyr was 0.23 ± 0.23 bar (2σ error) (Supplementary Information).

Code availability. Matlab code used in this manuscript to analyse the data is available in the Supplementary Information.

References

30. Hersterberg, T., Moore, D. S., Monaghan, S., Clipson, A. & Epstein, R. in *Introduction to the Practice of Statistics* (eds Moore, D. S. & McCabe, G. P.) (W. H. Freeman, 2012).

nature geoscience

SUPPLEMENTARY INFORMATION

DOI: 10.1038/NGEO2713

Earth's air pressure 2.7 billion years ago constrained to less than half of modern levels

Sanjoy M. Som[1*†], Roger Buick[1], James W. Hagadorn[2], Tim S. Blake[3], John M. Perreault[1†], Jelte P. Harnmeijer[1†] and David C. Catling[1]

Supplementary text

1. Sample localities

Samples from the top and bottom of 5 stacked flows were obtained from the Boongal Formation on the banks of the Beasley River (-22° 43' 30.54006", 117° 19' 13.21896"). The top and bottom of two further flows were also sampled, making 7 flows in all: one further up stratigraphy in the Bunjinah Formation ("Beasley River north"; -22° 41' 15.41473", 117° 20' 16.27100") and one at the Moona Well locality (-22° 45' 15.87449", 117° 25' 54.39339"), along strike from the Beasley River locality about 12 km east. Those localities are mapped in Fig. 1.

2. Marine-terrestrial transition recorded at the Beasley River locality

The Beasley River subaqueous-subaerial transition is interpreted as a marine-terrestrial regression for three reasons. Firstly, the lower surface of the lowermost flow as the Beasley River locality intrudes hyaloclastites (Fig. 2b) with lobate, downwards-penetrating (~20°) lava toes (Fig. 2a) rimmed by cracked glassy margins extending several meters into the underlying sediment. These characteristics are typical of subaerial lava interacting with unconsolidated wet sediment in a beach environment on a lava delta[31]. Secondly, the western-most expression of the Boongal and Bunjinah Formations crop out near Mt. McGrath, while the Bunjinah's eastern-most outcrop is in the Robertson Range. The Boongal Formation eastern-most outcrop is at Deadman Hill, 130 km west of Robertson Range. At all of these locations, the facies are subaqueous. Mt. McGrath and the Robertson Range are separated by ~450 km. Their subaerial equivalents, the Kylena and Maddina Formations, first outcrop ~90 km north of both localities. The great lateral extent of this transition strongly suggests an ocean-sized body of water. Thirdly, the 1000 m thick pillow basalts characterizing the lower Boongal Formation[16] were most likely deposited in a deep body of water such as an ocean. Thus, the subaqueous-subaerial transition at the Beasley River locality evidently represents lava solidification at sea level.

3. Age of samples

The most recent dating of the Fortescue Group by Blake et al.[32] focused on rocks from the Nullagine Synclinorium. Because stratigraphic correlations between formations in the north Pilbara and southwest Pilbara have been suggested, but not confirmed, attributing ages determined for these northern Pilbara rocks to the Boongal and Bunjinah Formations in the southwest Pilbara is problematic. However, Blake et al.[32] studied major- and trace-element distributions in Fortescue Group basalts from the Nullagine Synclinorium and his "package 6", comprising the upper Kylena Formation, geochemically resembles our samples (Table S1) from the Boongal Formation as illustrated in Fig. S1. This strongly suggests a genetic link between northern Pilbara rocks and their southern equivalents. Unfortunately "package 6" is the one package Blake et al.[32] were not able to date. "Package 5" from the lower Kylena is dated at 2741 +/- 3 Ma while the base of "package 7" sampled at the base of the Tumbiana Formation is dated at 2727 +/- 5 Ma. However, because the unconformity between "package 5" and "package 6" is cryptic and likely does not represent a significant time interval, and may not be present at all in the subaqueous southern Pilbara stratigraphy, an age of 2.74 Ga is assigned to the Boongal formation.

4. Flow selection criteria

Vesicular lava paleobarometry can only be applied to lava flows satisfying specific criteria[8]. The criteria are i) flow thickness of <2.5 m; ii) simple amygdale zonation with only a UVZ and LVZ and lacking sharply bounded interior

vesicular zones; and iii) no evidence of post-eruption gas addition in the form of pipe vesicles[33]. These strict criteria reduced the analyzed sample set to three flows: flows 2, 3 and 5 of the Boongal Formation at Beasley River (Figs. 1 and 2). Flow 1 was highly irregular in thickness due to its lava toes, flows 4 and 7 lacked an internal massive zone suggesting that they had been deflated, and flow 6 contains pipe vesicles and has thus suffered gas addition, as described below. We followed published methodology[8] in sampling cores a few centimeters below the top and above the bottom to avoid lava flow chilled margins.

5. Description of sampled flows

Beasley River

Flow 1: Flow 1 (-22° 43' 30.89403", 117° 18' 58.77616") does not have a planar basal exposure at the Beasley River outcrop locality, being deformed instead into lava toes, and thus was not sampled because of its extremely irregular thickness. At the base of the exposure, vesicularity is 10% increasing monotonically to 30% at the top.

Flow 2: Flow 2 (-22° 43' 30.47501", 117° 19' 13.21881") is 2.24 m thick (Fig. S2, S3a). It has a 4 cm greenish chilled margin at its base with weak internal zoning (no amygdales). Contact with the crystalline basalt of Flow 1 is sharp over 1 mm, with no interstitial hyaloclastic breccia (Fig. S3b). Vesicularity at base is ~3%, with dominantly chloritic (some quartzose) amygdales 1 - 3 mm in diameter. Vesicularity decreases to 1% with amygdales 1 - 2 mm in diameter above 10 cm. Rare coalescing amygdales 1 - 2 cm in diameter appear at 75 cm. Flow 2 is characterized by a zone of large ovoid to amoeboid cavities appearing 1.35 m above the base, which are typically 20 cm across and lined by 3 mm fuchsitic chert with drusey megaquartz or (rarely) calcite fillings. Those voids are associated with chloritic ovoid to irregular coalesced amygdales 2 - 5 mm in diameter and a vesicularity of 5%. They are irregularly developed along strike with some parts only having a few very large (6 cm tall x 20 cm wide) quartz-filled lensoid voids, others have clusters of 8% 5 mm sub-spheroidal amygdales up to 0.5 mm in diameter across. Abundance of amoeboid cavities increases upward in some areas to 20 cm from the flow top (Fig. S2. At a height of 1.65 m from the base, the flow becomes highly amygdaloidal (35%) with 4 - 12 mm in diameter amygdales, with as much as 25% of them being amalgamated (Fig. S2). This continues to 1.85 m above the base where vesicularity decreases markedly to 3%, but gradually increases again to 10% at the flow top, where amygdales are spheroidal and typically 3 - 6 mm in diameter, except for rare lenticular quartz-filled voids (1x4 cm). The flow's upper surface is characteristic of billowy pahoehoe with undulations 35 cm wide and 10 cm of relief with the top 1 cm containing 20% stretched amygdales 4 to 20 mm in length aligned along the undulation crests. No evidence of hyaloclastite, perlitic cracking or other aqueous alteration is visible at the surface of the flow. Lava inflation tends to result in nested units with their own vesicular zones interior to the lava, i.e., multiple layers of zones of small vesicles that were introduced by interior inflow after the exterior cooled. Such zones were not seen in Flow 2. In addition, no evidence of external gas charge such as pipe vesicles was observed. Flow 2 was characterized as simply emplaced and thus suitable for analysis.

Flow 3: Flow 3 (1.52 m thick), illustrated in Fig. S4, is fully exposed in several places at the Beasley River locality (-22° 43' 30.47600", 117° 19' 12.72801"). Its base is characterized by a 1.2 cm greenish glassy chilled margin, and is typically separated from the underlying flow 2 by a 1 cm weathered gap (Fig. S4). The base is further characterized by a

low vesicularity of 2% with chloritic amygdales 1 - 3 mm in diameter. Scattered amoeboid quartz-filled voids (3 x 7 cm) appear 50 cm from the base. Vesicularity increases markedly at 75 cm to 20% with sub-spheroidal quartz-filled amygdales 3-10 mm in diameter. This horizon is also characterized by amoeboid voids filled with quartz, fuchsitic chert, chlorite, and calcite. Typical voids range from spheroidal 1 cm in diameter to amoeboid 3 x 10 cm. Vesicularity increases to 35% within the top 30 cm. Amoeboid structures disappear in the top 10 cm of the flow, which has a vesicularity of 30% with spheroidal quartz-filled amygdales 2 - 8 mm in diameter, located in a brown glassy margin. The top of flow 3 is similar to flow 2, with billowy undulations 7 x 30 cm with 3 x 35 mm stretched amygdales in outer centimeter that are aligned along crest axes. No evidence of multiple layers of zones of small vesicles characteristic of lava inflation was found. Furthermore, the flow was devoid of pipe vesicles characteristic of external gas charge. As such, Flow 3 was characterized as simply emplaced and suitable for analysis.

Flow 4: Flow 4 (1.78 m thick), illustrated in Fig. S5, is fully exposed in two places at the Beasley River locality (-22° 43' 30.57293", 117° 19' 13.04375"). Similar to Flow 3, it has a 1 cm erosional gap between its base and the top of Flow 3. There is no evidence of a chilled margin, and the flow base is characterized by a vesicularity of 3%, with spheroidal chloritic amygdales 1 - 3 mm in diameter. This distribution in size and vesicularity is found up to 80 cm above the base, where large (5 x 12cm) lensoid to amoeboid voids filled with quartz-fuchsitic chert and calcite appear in a 25 cm thick zone. These voids occupy 5% of this horizon, but are not interconnected. Vesicularity increases in this same horizon to 5% with amygdales 3 - 5 mm in diameter. The large voids disappear in the top 50 cm but 1 - 2 cm in diameter amoeboid amalgamated vesicles become common, forming 5% of the rock, while 20% is occupied by spheroidal vesicles 3 - 6 mm in diameter. Vesicularity increases in the top 15 cm to 25%, where spheroidal quartzose and chloritic amygdales 2 - 5 mm in diameter prevail in the absence of coalesced amygdales. The top surface of the flow is somewhat foliated parallel to bedding, and no stretched amygdales are evident. The surface is very flat (relief 0.5 cm) compared with the underlying flows, and no hyaloclastite, cracking or perlitic fractures are observed. The fact that this flow does not have a massive zone suggests that this flow was not simply emplaced, perhaps having suffered deflation, and so it was deemed unsuitable for analysis.

Flow 5: Flow 5 (0.93 m thick), illustrated in Fig. S6, is fully exposed in one location (-22° 43' 30.44299", 117° 19' 12.97333"). Its base has a 5 cm erosional gap with chalcedony veins (0.5 cm wide), but no evidence of a chilled margin. The basal few centimeters of the flow is further characterized by 3% spheroidal chloritic amygdales1 - 3 mm in diameter, passing upward into a sparsely amygdaloidal massive zone. At a height of 45 cm above the base, scattered amoeboid to lenticular quartz-chlorite filled voids occupy 5% of rock, the largest void being 5 x 10 cm, but none are interconnected. At that same level, sub-spheroidal amygdales 2 - 4 mm in diameter increase to 5% of the rock. At 65 cm above the base, the large voids disappear and vesicularity increases to 10%, with sub-spheroidal quartzose and chloritic amygdales 3 - 8 mm in diameter. This same horizon is also characterized by quartz-chlorite filled amoeboid (1 x 2 cm) coalesced amygdales with a vesicularity of 2%. Vesicularity increases in the top 5 cm to 20% with spheroidal amygdales 3 - 6 mm in diameter, and no amoeboid voids are present. Stretched amygdales are absent from the flow's top surface. It is nearly planar (3 cm relief), with no hyaloclastite or perlitic fracturing. Flow 5 is overlain by Flow 6, which is at least 7.3 m thick, but disappears into a rubbly outcrop. Like Flows 2 and 3, Flow 5 lacked nested units containing individual vesicular zones interior to the lava flow. In addition no sources of external gas charge like pipe vesicles were observed. Flow 5 was thus characterized as simply emplaced and suitable for analysis.

Beasley River North (Flow 6)

This flow (1.04 m thick), illustrated in Fig. S7, is located north of the Beasley River locality (-22° 41' 15.41473", 117° 20' 16.27100") where Flows 1-5 are found, and lies stratigraphically higher in the Bunjinah Formation. Its base is characterized by a 5 cm thick 15% vesicular zone with spheroidal amygdales 3 – 10mm in diameter. This zone underlies a 30 cm horizon containing scattered 10 cm wide x 15 cm long pipe amygdales in addition to 1% vesicular spheroidal amygdales 2 – 10mm in diameter. Above the pipe amygdales, vesicularity increases to 20%, with spheroidal amygdales 2 - 20 mm in diameter accompanying 5% quartz-filled laminoid to amoeboid coalesced amygdales up to 30 mm across. This horizon is laterally discontinuous. The flow is capped by a 5 cm thick zone of spheroidal amygdales 3 - 8 mm in diameter, with a vesicularity of 15%. The flow surface is undulose with a 5 cm relief, and is strongly foliated. The presence of pipe amygdales indicates that this flow was not simply emplaced, with external gas charging of the flow during lithification. Consequently, this flow was deemed unsuitable for analysis.

Moona Well (Flow 7)

This flow (1.16 m thick) is located at Moona Well ~12 km east along strike from the Beasley River locality (-22° 45' 15.87449", 117° 25' 54.39339"). The flow has a coarsely amygdaloidal base with a vesicularity of 10% with spheroidal amygdales 2 - 5 mm in diameter. Vesicularity drops to 5% 85cm above the base. From 85 cm to 100 cm, irregular amoeboid amygdales form 3% of the rock. The top 16 cm are a 30% vesicular scoriaceous horizon characterized by spheroidal to lobate 5 - 10 mm amygdales. The flow top is slightly undulating with 7 cm of relief over 50 cm. The Moona Well flow has been extensively metasomatized and perhaps for this reason, the amygdales could not be distinguished by our automatic X-ray detection routine which precluded analysis. But as the flow lacks a relatively unvesiculated massive zone, it could have been deflated, thus rendering it unsuitable for analysis anyway.

5. Error analysis

The pressure equation is (from Eq. 1):

$$P_{atm} = \rho g H \, (V_r - 1)^{-1} \, , \tag{S1}$$

where $V_r = V_t / V_b$. V_t is the mean amygdale volume at the top of the flow, and V_b is the mean amygdale volume at the bottom of the flow. Each independent term *n* in the equation will have an independent sampling error $(\delta P_{atm})_n$ associated with it, contributing to the overall total error δP_{atm}, where

$$\delta P_{atm} = \sqrt{(\delta P_{atm})_\rho^2 + (\delta P_{atm})_g^2 + (\delta P_{atm})_H^2 + (\delta P_{atm})_{V_b}^2 + (\delta P_{atm})_{V_t}^2} \tag{S2}$$

and

$$(\delta P_{atm})_n = \left(\frac{\partial P_{atm}}{\partial n}\right) \delta n \, .$$

As such, each element in eq. S2 can be expressed as (S3a-e):

$$(\delta P_{atm})_{\rho} = \left(\frac{\partial P_{atm}}{\partial \rho}\right)\delta\rho = \left(\frac{gH}{\frac{V_t}{V_b} - 1}\right)\delta\rho$$

$$(\delta P_{atm})_{g} = \left(\frac{\partial P_{atm}}{\partial \rho}\right)\delta g = \left(\frac{\rho H}{\frac{V_t}{V_b} - 1}\right)\delta g$$

$$(\delta P_{atm})_{H} = \left(\frac{\partial P_{atm}}{\partial \rho}\right)\delta H = \left(\frac{\rho g}{\frac{V_t}{V_b} - 1}\right)\delta H$$

$$(\delta P_{atm})_{V_t} = \left(\frac{\partial P_{atm}}{\partial V_t}\right)\delta V_t = -\left(\frac{\rho g H}{V_b\left(\frac{V_t}{V_b} - 1\right)^2}\right)\delta V_t$$

$$(\delta P_{atm})_{b} = \left(\frac{\partial P_{atm}}{\partial V_b}\right)\delta V_b = \left(\frac{V_t \rho g H}{V_b^2\left(\frac{V_t}{V_b} - 1\right)^2}\right)\delta V_b$$

where $\delta\rho$, δg, δH, δV_b and δV_t are the measurement errors. The acceleration due to gravity g is obviously known to high accuracy, so we assign $\delta g = 0$. We further set $\delta\rho = 100$ kg m^{-3}, and a conservative $\delta H = 5\%$ of lava flow thickness H to account for the variability in thickness observed in the field.

Here we describe how to calculate δV_b and δV_t. The distribution of the volume of vesicles in basalts is generally found to be close to log-normal[34] and, as shown below, we find that our distributions also form an approximately log-normal distribution. The physics of why the distribution of gas bubbles best fit the log-normal has been discussed to some extent elsewhere (see references in Ref. 34). In essence, there is a fixed linear growth factor when vesicles form. So, the bubbles that randomly grow larger than average will be a factor of 'x' larger (multiplicative), whereas the ones that randomly grow smaller than average will be a factor of 'x' smaller (divisional). This results in an approximately log-normal distribution about the mean. In contrast, a linear normal distribution is where the random perturbations about a mean are additive or subtractive (not multiplicative or divisional).

Standard statistical techniques require data that are normal (or Gaussian). Because the vesicle volume data tend to be roughly log-normal, Proussevitch et al.[34] recommend converting vesicular volumes to their logarithms, which converts the roughly log-normal distributions to roughly normal distributions. Each distribution plotted in Figs S12 – S14 is accompanied by a normal quantile plot that graphically represents how close the distribution is to normality, with a correlation coefficient r = 0.9976 being the critical correlation coefficient (from NIST statistical tables) required to accept the null hypothesis that the data came from a normal distribution. Those plots show that most outcrop distributions cannot be statistically determined to come from a normal distribution, making the use of standard statistical theory difficult. Consequently, we use bootstrap statistics to estimate the mean vesicle volume from the roughly normal distribution[30]. Applying 2000 bootstrap resamples and plotting their means reveal, from the resulting normal quantile plots (plotted in Figs S12 – S14), that the distribution of the mean of means is normal, (verifying the

Central Limit Theorem), and allowing the use of standard statistical theory such as the ~2σ spread for the 95% confidence interval. The mean of this latter distribution is the best estimate for the mean of amygdale population, and the standard deviation a measure of its error[30]. This error associated with the mean vesicle volume can then be used with other sources of error in standard error propagation (which assumes normally-distributed errors) as discussed above. Our MATLAB code for the bootstrapping is available in the online Supplementary Information. If large (or small) vesicles skew the mean from the mode do exist in the original dataset, they will simply increase the standard deviation of the Gaussian representing the mean of 2000 sample means. Outliers are thus taken into account in the statistics.

Converting these results back to linear space is the last step to obtain δV_b and δV_t. The calculation is as follows[17]:

Let μ equal the mean of the means of the bootstrapped distributions at either the flow top or bottom, and σ_μ the standard deviation of that Gaussian. Let $\log(V_m) = \mu$, where V_m is the population mean in linear space, from which:

$$V_m = 10^{\mu}. \tag{S4}$$

The error $\delta V_{t,b}$ in V_m due to the error σ_μ in μ is then expressed as:

$$\delta V_{t,b} = \{ [(\partial V_m/\partial\mu)\sigma_\mu]^2 \}^{1/2} \tag{S5}$$

The term $(\partial V_m/\partial\mu)$ can be written as $10^{\mu}\ln(10)$ from the relationship:

$$\partial a^x/\partial x = a^x \ln(a) \tag{S6}$$

where a is a constant and x is a generic independente variable. Therefore, the volumetric error in the mean is expressed as:

$$\delta V_{t,b} = 10^{\mu}\ln(10)\sigma_\mu \tag{S7}$$

Eqn. S7 corrects a typo in eqn. 10 of Ref. 17.

This method of error calculation is preferred because it produces a single standard deviation value when back-transforming from logarithmic to linear, which can be inserted as δV_b and δV_t in eqn. S3d,e. Another method involves back-transforming the error upper bound (mean + standard deviation) independently from the error lower bound (mean – standard deviation), creating asymmetric error bars in the linear domain, making error propagation calculations challenging. For the 95% confidence interval, we multiply the standard deviation by 1.96 (i.e., ≈2σ):

$$V_{m\_upper} = 10^{(V_m + 1.96\sigma_\mu)} \tag{S8a}$$

$$V_{m\_lower} = 10^{(V_m - 1.96\sigma_\mu)} \tag{S8b}$$

As shown in Table S2, eqn S7 is an excellent approximation. Thus, it is reasonable to use the mean Gaussian error in linear space from eqn. S7 in error propagation (which assumes normally-distributed errors).

Sahagian et al.[8] use the mode of the distribution representing the sample vesicle size distribution, rather than a bootstrapped mean that we use here. They do so because the quantity of vesicular data they obtain allows them to create high resolution histograms with dozens of bins representing thousands of vesicles making the mode readily obtainable. The use of the mode allows neglecting the large quantities of small vesicles, in addition to the very large ones, as these outliers – while potentially skewing the mean – do not affect the mode. In our case, with only hundreds of vesicles, the mode is not necessarily obvious from the histogram alone. As such, we formulate a different, more robust approach to handle size-distribution data, particularly in the way errors are calculated as described above. Our formulation includes all outliers. To compare our method with that of Sahagian et al.[8], we calculate air pressure using estimates of the mean, median, and mode of the log distribution, which is shown in Table S3 and plotted in Fig. S8). The results show that our method and its associated error encapsulates the other measurements methods, including that of Sahagian et al.[8].

To calculate air pressure using the mode as does Ref. 8, our smaller datasets of amygdale volume demand a method that is histogram-independent. Because the data stems from a continuous distribution, the mode in its traditional implementation cannot be used, so we use a Kernel Density Estimator tool[35] to identify it (Figs. S9 - S11). If the KDE returns a bimodal distribution, the corresponding vesicle volumes associated with those modes are compared, and the largest is selected as the mode for computation of air pressure. This is following the recommendation of Ref. 33 who note that a smaller mode of two is an artifact sometimes created because of secondary coalescence of smaller vesicles and therefore not representative of the true mode. The MATLAB code for determining the Kernel Density is available on the MATLAB File Exchange and is included in the online Supplementary Information.

In their calculation of error, Sahagian et al.[8] approximate the effective error in pressure by calculating the error based on a representative vesicle of 1 mm in diameter. In contrast, all the amygdales are taken into account in our bootstrap estimate of the population mean and its error, and no approximations are taken. Our error is simply the standard deviation of the Gaussian representing the mean of the 2000 bootstrapped datasets, and applies to the entire population of amygdales. The average pressure calculated from the three flows suggests that the sea-level air pressure at 2.74 Ga was 0.22 ± 0.24 bar (2σ error). To correct for unrealistic negative pressures at the lower limit, we used a renormalized confidence interval method[36] and obtained 0.23 ± 0.23 bar (2σ error) where the mean and uncertainty are calculated subject to the Bayesian prior that absolute pressure cannot be negative. The MATLAB code for determining air pressure based on vesicle dimensions is included in the online Supplementary Information.

For additional details on applying bootstrapping to a tomography sample of vesicle volumes and error analyses, see Ref. 17. The results of applying the bootstrap statistics to the flows are plotted in Figs S12 - S14.

No error is assumed for the elevation of the outcrop due to its clear stratigraphic identification at sea-level (Section S2). In fact, any lava flow within 800 m of sea level will measure air pressure to within 10% of a ~0.2 bar sea-level pressure.

6. Estimates of modern geological N fluxes

The Phanerozoic geological nitrogen fluxes in the main text were estimated using the N/C ratio of various carbon reservoirs or outgassing fluxes and applying the N/C ratio as a scaling factor to well-known carbon fluxes[19]. Global carbon fluxes are the most studied of any chemical element, so our approach gives N flux estimates with uncertainties. However, the subduction flux of N and the mid-ocean ridge flux of N described in detail below were literature estimates that used other techniques. In the Phanerozoic, the key geologic N source fluxes are outgassing (volcanic and metamorphic) and oxidative weathering of continental organic matter, which releases nitrate that undergoes biological denitrification essentially instantaneously on geologic timescales. The N sink flux is through the burial of organic matter. A key conceptual point is that the only forms of N that can accumulate in the long term (over geologic timescales) are N_2 in the atmosphere or reduced N in rocks. The biosphere is a tiny, transient reservoir. It is for this reason that we must consider oxidative weathering and rapid denitrification as an N source to the atmosphere on geologic timescales.

We estimate the N outgassing flux as follows. A literature review[37] indicates that the average CO_2 outgassing from all sources is 7 ± 3 Tmol C/yr (see in particular Table 4.1 in Ref. 37). Based on directly measured average N/C ratios in subaerial volcanic and metamorphic gas emissions[19], the N flux outgassing from arcs, hotspots, and metamorphism is 0.17 ± 0.07 Tmol N/yr, scaling from the C outgassing flux. Additionally, 0.008 ± 0.003 Tmol N/yr is outgassed from mid-ocean ridges, according to helium-nitrogen systematics[38]. The total N outgassing flux from the sum of these components is 0.18 ± 0.07 Tmol N/yr.

We estimate N burial and N weathering fluxes as follows. Analyses of sedimentary geochemical data reveal estimates of the organic carbon oxidative weathering flux as 7.5 ± 1.7 Tmol/yr and organic carbon burial flux as 10 ± 1.7 Tmol/yr[27]. Based on N/C data for Phanerozoic shales and continental organics[19], we estimate the weathering N flux as 0.15 ± 0.03 Tmol N/yr and the organic burial N flux as 0.4 ± 0.2 Tmol N/yr. The fraction of buried N that goes into subduction zones is relatively small[20], 0.094 ± 0.015 Tmol N/yr (compared to a value of 0.16 Tmol N/yr estimated in Ref. 39) and within the noise of the uncertainty of the organic burial N sink. The net subduction flux is within error bar of zero, if we take the value of Ref. 39 for the flux of N fed into subduction zones.

Overall, the total N source flux (0.33 ± 0.08 Tmol N/yr) and N sink flux (0.4 ± 0.2 Tmol N/yr) balance within the uncertainty. In fact, modeling suggests that the Phanerozoic mass of N_2 in the atmosphere probably varied < 1% [19].

The main text discusses the key differences in the anoxic Archaean. Firstly, there are convincing reasons why the N source flux was smaller than today. The lack of an N oxidative weathering flux meant that the total N source flux would have been halved based on the fluxes given above. Possibly (but very speculatively), the degassing of N was smaller too if the source regions for gases from arc volcanism were at a lower redox state than today because this would stabilize nitrogen in silicates against volatilization[29]. Secondly, in steady state balance, the global N sink flux must have been smaller to balance a relatively diminished N source flux. Analysis of the carbon isotope record shows that organic carbon burial is consistent with a smaller N sink in the Archaean as follows: in a generalized least squares analysis of C

isotopes, the fraction of carbon buried shows an increase of ~30% from the Archaean (0.15 ± 0.01 at 3.8-2.5 Gyr) to the Phanerozoic (0.22 ± 0.02 at 0.54-0 Gyr)[40]. Assuming the same N/C scaling, the Archaean N sink from organic burial may have been similarly smaller by ~30% compared to the Phanerozoic. Clearly, this is smaller than the minimum expected decrease of the N source flux (~50%). However, in the Archaean there would be a significant sink that is absent in today's oxygenated world. Ammonium, would be the dominant nitrogen species in the anoxic deep sea[27]. Ammonium can readily substitute for potassium ions in clay minerals and provides a path for N to be transferred into the solid Earth[41]. Biological anaerobic ammonium oxidation ("anammox") is a pathway that in principle could oxidize ammonium directly to nitrogen. However, this mechanism requires nitrite (NO_2^-), which would have been negligible in the Archaean deep ocean (as it is in the modern Black Sea). Furthermore, ammonium-rich Archaean metasediments[26,28] indicate that N_2 released by anammox was negligible. Consequently, a considerable increase in the fraction of nitrogen that entered crustal minerals and was subducted could make up the balance of the N sink flux. Nitrogen-enriched ~3.5 Gyr placer diamonds may record this period of high N subduction[42]. Importantly, because such a nitrogen sink should depend on the concentration of N in the atmosphere-ocean system, the steady-state balance of N sources and sinks would tend to favor lower pN_2 in the atmosphere than today.

7. Nitrogen draw-down

We considered both abiotic and biological mechanisms that may have been responsible for sequestering nitrogen from the early Earth's atmosphere. Today it is estimated that there is ~2.1±1 bar of N_2 in the mantle and crust[4] with only 0.8 bar of N_2 in the air. Most mantle nitrogen probably degassed during the first 200 Myr of Earth's history from a magma ocean[21] because of its low solubility in silicate melts[43]. Some was evidently later removed from the air and returned to the solid Earth.

Non-biological atmospheric nitrogen removal processes include fixation by lightning[22], and HCN formation and deposition[23]. In an anoxic atmosphere, N_2 reacts with CO_2 under the influence of lightning to form nitric oxide (NO) and carbon monoxide (CO) (Ref. 22). Subsequently, NO further reacts to form a soluble nitrosyl hydride (HNO), which can rain out of the atmosphere and disproportionate into forms of nitrogen that can be sequestered by burial[44]. However, the flux of nitrogen fixed by lightning is very low, not more than 0.021 Tmol N/yr depending on the CO_2 mixing ratio[22]. If this abiotic nitrogen fixation flux was uniform for the 1.8 Gyr from Earth's origin to Boongal deposition with none returning to the atmosphere, this mechanism could only sequester ~0.1 bar of N_2. The other abiotic draw-down mechanism via HCN arises from N atoms that react with methylene (CH_2) and methyl (CH_3) radicals derived from the photolysis of methane[23]. Although the reaction-rate constants are uncertain, the nitrogen removal rate is estimated to be small, similar to that by lightning[24]. Thus, the fluxes of purely abiotic fixed nitrogen are evidently insufficient to explain low atmospheric pN_2 during the late Archaean.

A hypothesis for why the early atmosphere (before 2.7 Gyr ago) may have lost N_2 relative to today is as follows. In the Archaean ocean, the dominant form of N in seawater was ammonium, given anoxic geochemical speciation[1,27] and enhanced levels of ammonium in marine sediments that are inferred to have been derived from clay minerals[26,28]. Biological nitrogen fixation has been proposed to date back even to the last common ancestor of extant life based on phylogenetics[45], although that idea is controversial and disputed. Nonetheless, given the antiquity of biological nitrogen

fixation going back to 3.2 Gyr[25] or even 3.8 Gyr[26] from geochemical evidence, atmospheric nitrogen gas would be efficiently transformed to dissolved ammonium by microbial ammonification after biological fixation. The estimated modern N fixation flux is > 1.43 Tmol N/yr, for example[24]. Seawater ammonium can be incorporated into phyllosilcate minerals because it substitutes for K^+, which ultimately transfers to other silicates[46,47]. Ammonium in silicates is refractory during high temperature processes unlike carbon[46], which returns to the atmosphere as CO_2 or CH_4 in a faster geologic cycle than nitrogen. Thus, nitrogen could plausibly have been sequestered into crustal and mantle minerals on the early Earth, leaving a thinner atmosphere than today.

We can gain additional insight from estimates of fluxes. Today, the input of N into subduction zones is estimated as ~0.094 Tmol N/yr[20]. If this flux were an order of magnitude greater in the Archaean due to efficient ammonium sinks into phyllosilicates, and all the ammonium entered the mantle, then the residence time of the equivalent present atmospheric level of nitrogen (2.8×10^8 Tmol N) against subduction would be 0.3 Gyr. It is reasonable to assume that in the absence of atmospheric oxygen the source of nitrogen released from oxidative weathering of organic matter would be greatly diminished compared to today's flux of ~0.15 Tmol N/yr[19]. However, outgassing (currently ~0.33 Tmol N/yr) would have maintained pN_2 at some lower level than today in dynamic balance.

The oxygenation of the atmosphere at ~2.4 Gyr likely caused a return of nitrogen to the atmosphere and, because the dominant form of N in the ocean changed to nitrate, the pathway to lose N to ammonium silicates was also diminished. The most obvious new source of N was oxidative weathering of organic material on the continents, releasing nitrate to rivers and the ocean where biological denitrification would return N_2 to the atmosphere. As mentioned above, oxidative weathering releases N from organic carbon[19] with a flux that we estimate as ~0.15 Tmol N/year. A more speculative possibility is that following the Great Oxidation Event (GOE), newly available oxidized species like Fe^{3+} and sulfates made their way to the mantle wedge by subduction[48], which may have shifted the redox balance allowing nitrogen to speciate from NH_4^+, which tends to stay in the solid phase, to N_2, which tends to be released to the atmosphere[29]. Thus, the flux of N_2 from arc volcanism may have increased as a feedback effect of the GOE if the source region's redox state changed. One can estimate, based on modern fluxes, how long a return to a 0.8 bar pN_2 would take from a N_2 dominant 0.5 bar atmosphere. Modern outgassing of nitrogen is ~0.18 Tmol N/year, which when summed with the flux from oxidative weathering, gives a release of ~0.33 Tmol N/year (following Ref. 19). Thus, ~0.3 bar N_2 (~1.08×10^8 Tmol N following Ref. 49) would be replenished in ~330 million years. This value is conservative because outgassing rates were likely greater in the Archaean owing to a hotter lithosphere and mantle. It is interesting that this duration would coincide with the time of 2.4-2.0 Gyr ago when there were major fluctuations in climate and the global carbon cycle, before the Earth system settled into the Proterozoic eon.

Overall, early Archaean (or even Hadean) burial of substantial quantities of biologically fixed nitrogen would support the hypothesis of Goldblatt et al.[4] that the nitrogen present in the mantle today was in the atmosphere at some point very early in Earth's history, but not as late as 2.7 Gyr.

References for Supplementary Materials

31. Cas, R. & Wright, J. V. *Volcanic Successions, modern and ancient: a geological approach to processes, products, and successions*. (Allen & Unwin, 1987).

32. Blake, T. S., Buick, R., Brown, S. J. a. & Barley, M. E. Geochronology of a Late Archaean flood basalt province in the Pilbara Craton, Australia: constraints on basin evolution, volcanic and sedimentary accumulation, and continental drift rates. *Precambrian Res.* **133,** 143–173 (2004).

33. Sahagian, D. & Proussevitch, A. Paleoelevation Measurement on the Basis of Vesicular Basalts. *Reviews in Mineralogy and Geochemistry* **66,** 195–213 (2007).

34. Proussevitch, A. Statistical analysis of bubble and crystal size distributions: Formulations and procedures. *J. Volcanol. Geotherm. Res.* **164,** 95–111 (2007).

35. Botev, Z., Grotowski, J. & Kroese, D. Kernel density estimation via diffusion. *Ann. Stat.* **38,** 2916–2957 (2010).

36. Cowen, S. & Ellison, S. L. R. Measurement uncertainty and confidence intervals near natural limits. *Analyst* **131,** 710–717 (2006).

37. Berner, R. a. *The Phanerozoic carbon cycle: CO2 and O2*. (Oxford University Press, 2004).

38. Marty, B. & Zimmermann, L. Volatiles (He, C, N, Ar) in mid-ocean ridge basalts: Assesment of shallow-level fractionation and characterization of source composition. *Geochim. Cosmochim. Acta* **63,** 3619–3633 (1999).

39. Johnson, B. & Goldblatt, C. The Nitrogen Budget of Earth. *Earth-Science Rev.* **148,** 150–173 (2015).

40. Krissansen-Totton, J. A statistical analysis of the carbon isotope record from the Archean to Phanerozoic and implications for the rise of oxygen. *Am. J. Sci.* **315,** 275–316 (2015).

41. Watenphul, A., Wunder, B. & Heinrich, W. High-pressure ammonium-bearing silicates: Implications for nitrogen and hydrogen storage in the Earth's mantle. *Am. Mineral.* **94,** 283–292 (2009).

42. Smart, K. A., Tappe, S., Stern, R. A., Webb, S. J. & Ashwal, L. D. Early Archaean tectonics and mantle redox recorded in Witwatersrand diamonds. *Nat. Geosci.* 1–6 (2016). doi:10.1038/NGEO2628

43. Wen, J. S., Pinto, J. P. & Yung, Y. L. Photochemistry of CO and H2O: analysis of laboratory experiments and applications to the prebiotic Earth's atmosphere. *J. Geophys. Res.* **94,** 14957–70 (1989).

44. Catling, D. & Kasting, J. in *Planets and Life: The Emerging Science of Astrobiology* (eds. Sullivan, W. T. & Baross, J. A.) 91–116 (Cambridge University Press, 2007).

45. Fani, R., Gallo, R. & Liò, P. Molecular evolution of nitrogen fixation: the evolutionary history of the nifD, nifK, nifE, and nifN genes. *J. Mol. Evol.* **51,** 1–11 (2000).

46. Boyd, S. Ammonium as a biomarker in Precambrian metasediments. *Precambrian Res.* **108,** 159–173 (2001).

47. Morse, J. & Morin, J. Ammonium interaction with coastal marine sediments: influence of redox conditions on K*. *Mar. Chem.* **95,** 107–112 (2005).

48. Evans, K. The redox budget of subduction zones. *Earth-Science Rev.* **113,** 11–32 (2012).

49. Trenberth, K. Global atmospheric mass, surface pressure, and water vapor variations. *J. Geophys. Res. Atmos.* **92,** 14815–14826 (1987).

Table S1: Major and trace element data for the various localities in this study. BR = Beasley river North, MW = Moona Well.

Sample	05015C	05018C	05020C	05022A	05023	05028
Date	23-Apr-10	23-Apr-10	23-Apr-10	23-Apr-10	23-Apr-10	23-Apr-10
Location	Flow 2	Flow 3	Flow 4	Flow 5	BR North	MW
Unnormalized Major Elements (Weight %):						
SiO2	56.48	67.36	53.64	56.16	54.91	47.86
TiO2	1.197	1.183	0.654	1.155	0.671	1.032
Al2O3	13.66	11.81	14.30	14.04	14.36	13.42
FeO*	8.87	6.31	8.73	10.38	7.94	12.35
MnO	0.115	0.070	0.149	0.147	0.140	0.225
MgO	5.14	2.97	6.17	5.22	5.49	3.56
CaO	4.97	3.01	7.84	3.75	7.92	7.80
Na2O	4.91	4.17	2.05	4.07	2.28	1.12
K2O	1.28	0.91	2.53	0.88	2.77	1.63
P2O5	0.187	0.139	0.075	0.135	0.077	0.162
Sum	96.81	97.94	96.14	95.94	96.57	89.16
LOI (%)	2.60	2.10	2.63	3.28	2.13	9.52
Normalized Major Elements (Weight %):						
SiO2	58.34	68.78	55.80	58.53	56.87	53.67
TiO2	1.237	1.208	0.680	1.203	0.695	1.158
Al2O3	14.11	12.06	14.87	14.64	14.87	15.05
FeO*	9.16	6.44	9.08	10.82	8.22	13.86
MnO	0.119	0.072	0.155	0.153	0.145	0.253
MgO	5.31	3.03	6.42	5.44	5.68	3.99
CaO	5.14	3.07	8.16	3.91	8.20	8.75
Na2O	5.07	4.26	2.13	4.24	2.36	1.25
K2O	1.32	0.93	2.64	0.92	2.87	1.83
P2O5	0.193	0.142	0.078	0.141	0.080	0.182
Total	100.00	100.00	100.00	100.00	100.00	100.00
Unnormalized Trace Elements (ppm):						
Ni	47	38	97	45	96	65
Cr	64	63	202	46	200	51
Sc	43	40	34	35	34	31
V	288	278	204	310	202	198
Ba	346	285	1080	300	1202	114
Rb	41	29	89	28	98	115
Sr	47	60	245	56	250	28
Zr	142	139	77	136	80	194
Y	22	24	16	25	17	35
Nb	8.7	7.9	5.7	8.0	4.6	12.2
Ga	10	10	16	12	15	16
Cu	9	53	74	39	70	23
Zn	88	62	71	108	69	72
Pb	3	3	4	3	5	4
La	24	20	12	23	12	29
Ce	50	37	28	41	24	60
Th	8	8	4	8	3	8
Nd	21	18	14	18	12	26
U	2	3	2	2	3	2
sum tr.	1263	1177	2273	1243	2395	1081
in %	0.13	0.12	0.23	0.12	0.24	0.11
sum m+tr	96.94	98.06	96.36	96.07	96.81	89.27
M+Toxides	96.97	98.09	96.41	96.10	96.86	89.30
w/LOI	99.58	100.19	99.04	99.39	98.99	98.82
if Fe3+	100.56	100.89	100.01	100.54	99.87	100.19

Major elements are normalized on a volatile-free basis, with total Fe expressed as FeO.

Table S2: Two methods of calculating errors. All values in mm^3. Only values for Upper Vesicular Zone shown. This table shows that transformation of the standard deviation from logarithmic to linear using Eq. 7 is a good approximation to the asymmetrical result (Eq. S8). The "single-value" is preferred as it allows effective error propagation in the calculation of air pressure error (Eq. S2, S3d,e)

Flow #	V_m (Eq. S4)	Combined error 2σ (2 x Eq. S7)	Upper-bound error (Eq. S8a)	Lower-bound error (Eq. S8b)
2	2.24	0.28	0.29	0.25
3	2.85	0.57	0.62	0.51
5	0.98	0.17	0.18	0.15

Table S3: Atmospheric pressure of each flow using different parameters. Air pressure is calculated given the mean, median and mode of the logarithmic distribution of amygdale sizes.

Flow #	Patm [bar] (log data)			Patm (bootstrap method)
	Mean	Median	Mode	
2	0.14	0.12	0.06	0.14
3	0.11	0.12	0.08	0.11
5	0.40	0.38	0.05	0.39

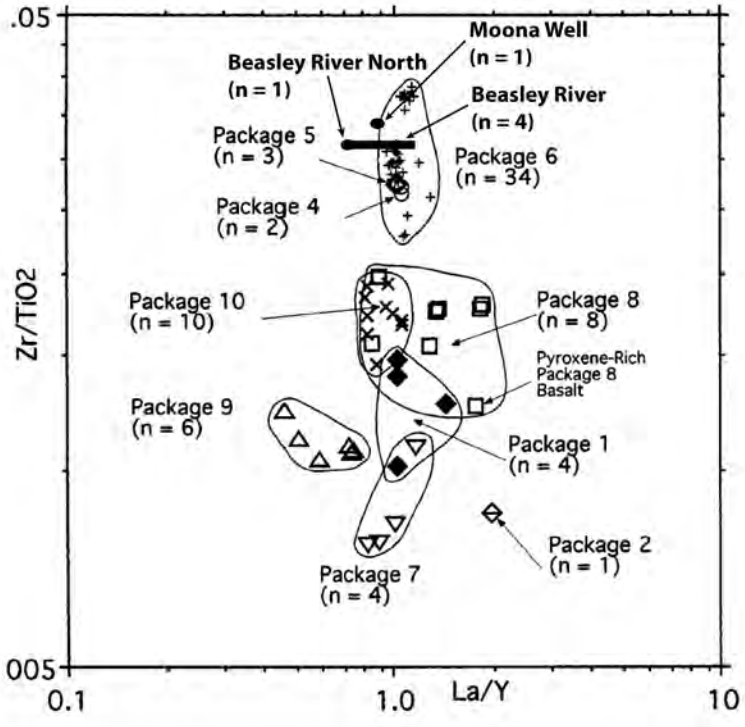

Figure S1: Geochemical results from the Beasley River samples overprinted on northern Pilbara results[32].

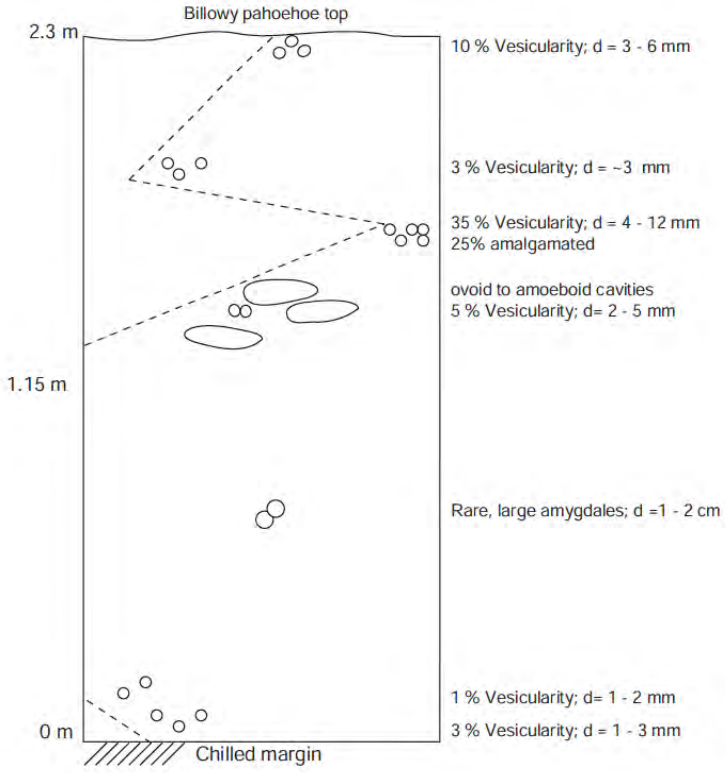

Figure S2: Cross-section diagram of Flow 2; dashed lines are illustrative of vesicularity trends.

a) b)

Figure S3: a) Complete section through Flow 2 – 33 cm long hammer for scale. b) Sharp contact between the top of Flow 1 (amygdale rich) and the base of Flow 2 (amygdale poor) – pocket knife for scale (Photos: S. Som)

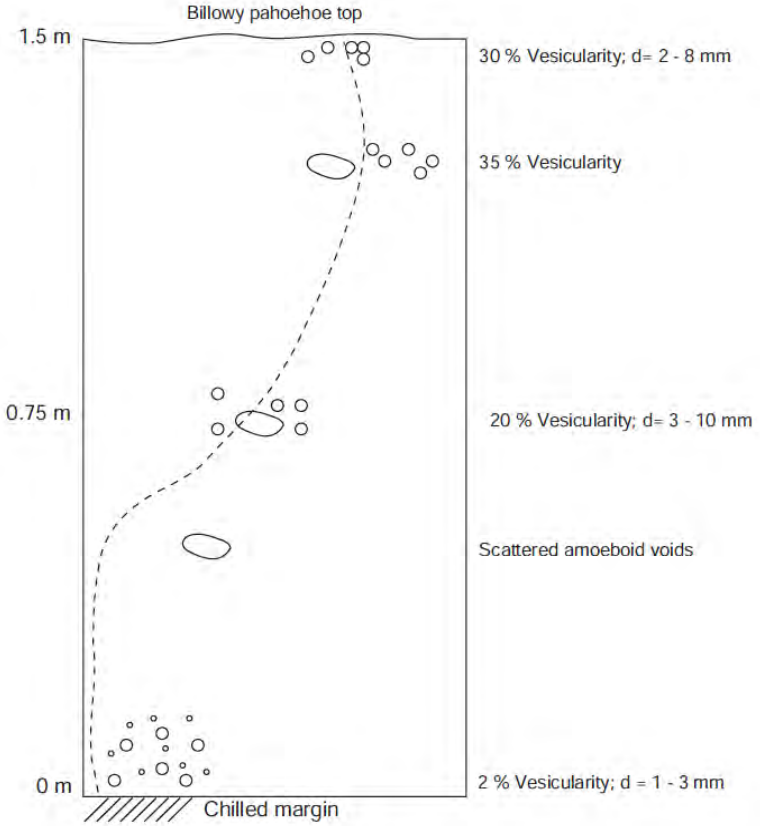

Figure S4: Cross-section diagram of Flow 3; dashed line is illustrative of vesicularity trend.

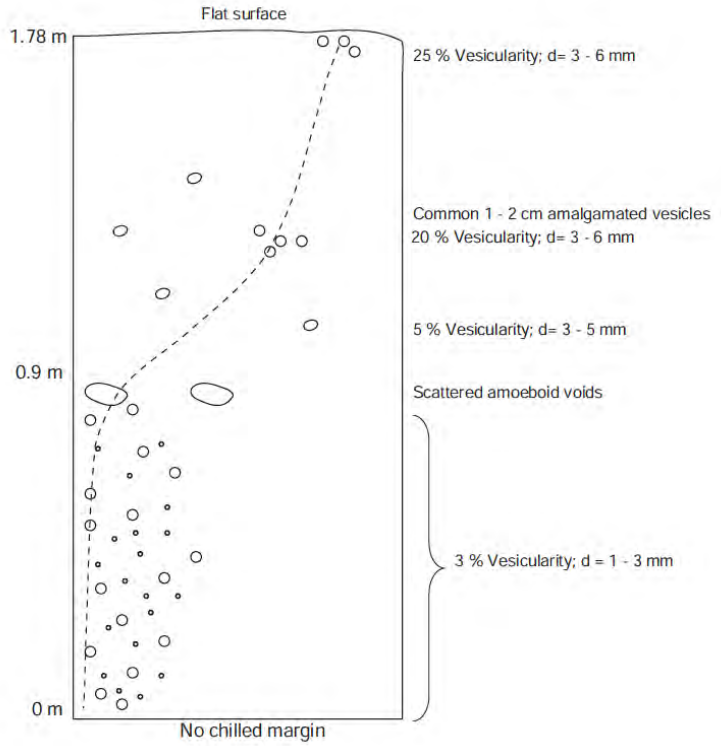

Figure S5: Cross-section diagram of Flow 4; dashed line is illustrative of vesicularity trend.

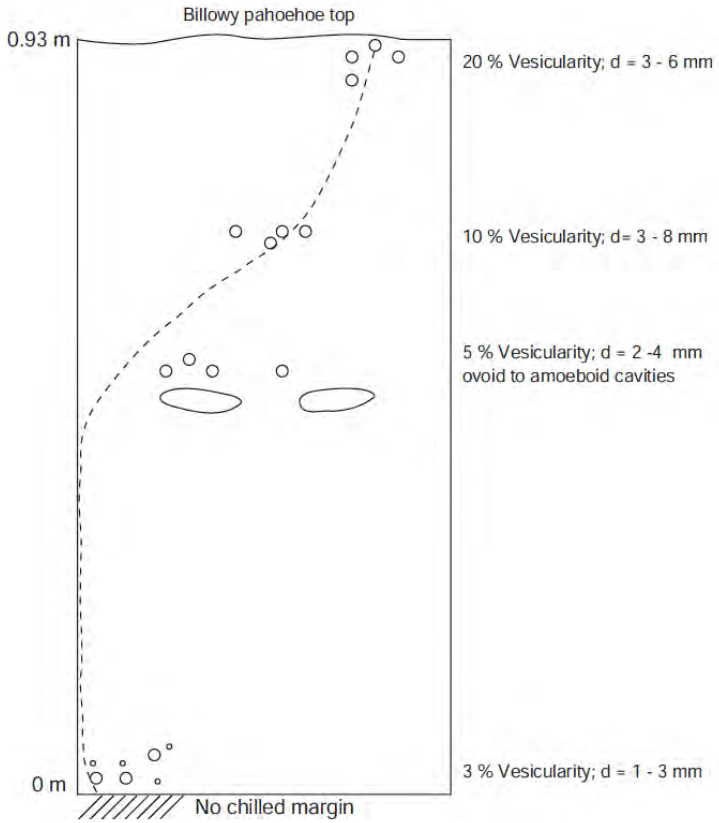

Figure S6: Cross-section diagram of Flow 5; dashed line is illustrative of vesicularity trend.

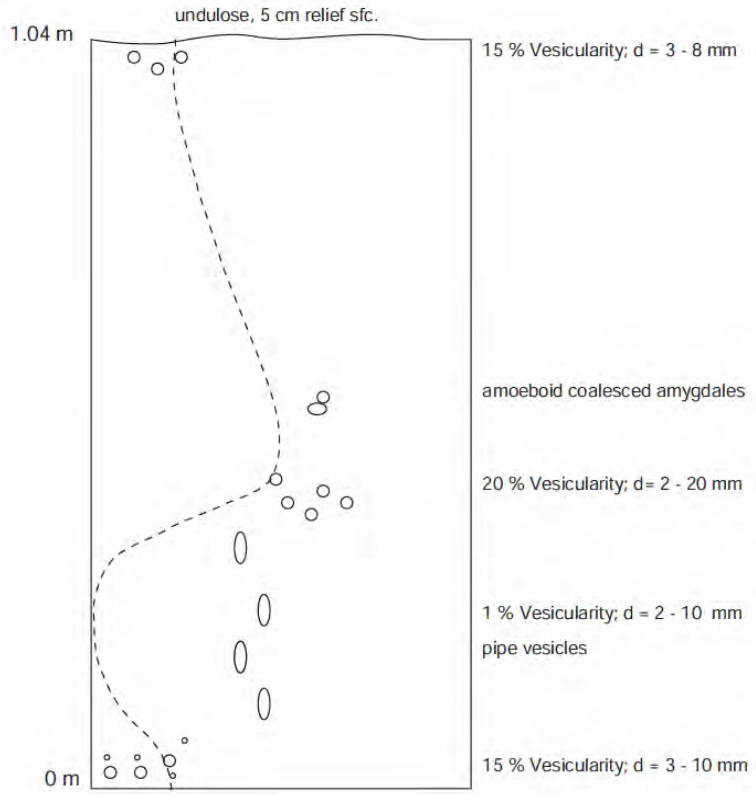

Figure S7: Cross-section diagram of Flow 6; dashed line is illustrative of vesicularity trend.

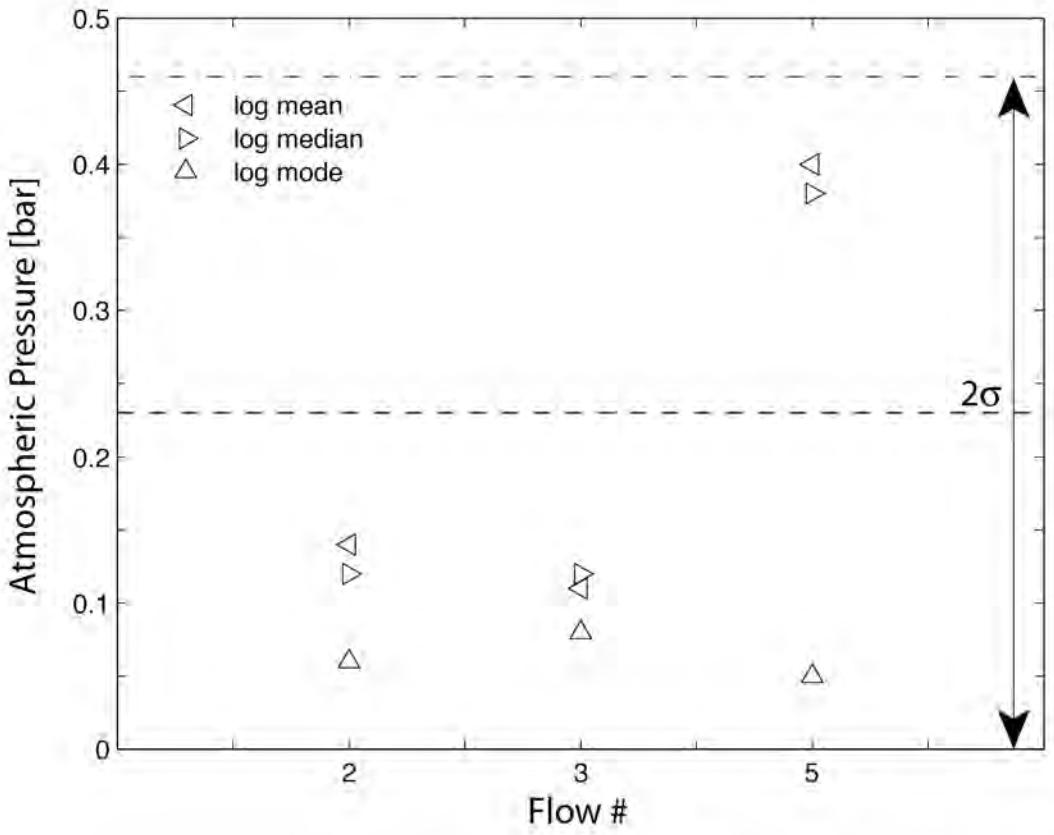

Fig. S8: Illustration of Table S1 showing atmospheric pressure (P_{atm}) results for each flow using different statistical measures of the central tendency of the log-normal vesicle distributions from lava flows 2, 3 and 5. The different statistical measures (see text) are labelled 'log mean', 'log median' and 'log mode', respectively. Using the method of a bootstrap sampling distribution of the mean, the result from the three flows combined is a mean atmospheric pressure of P_{atm} = 0.23 bar with a 2σ uncertainty of 0.23 bar. This bootstrap estimate encompasses all the other estimates within its 2σ uncertainty (or 95% confidence interval)..

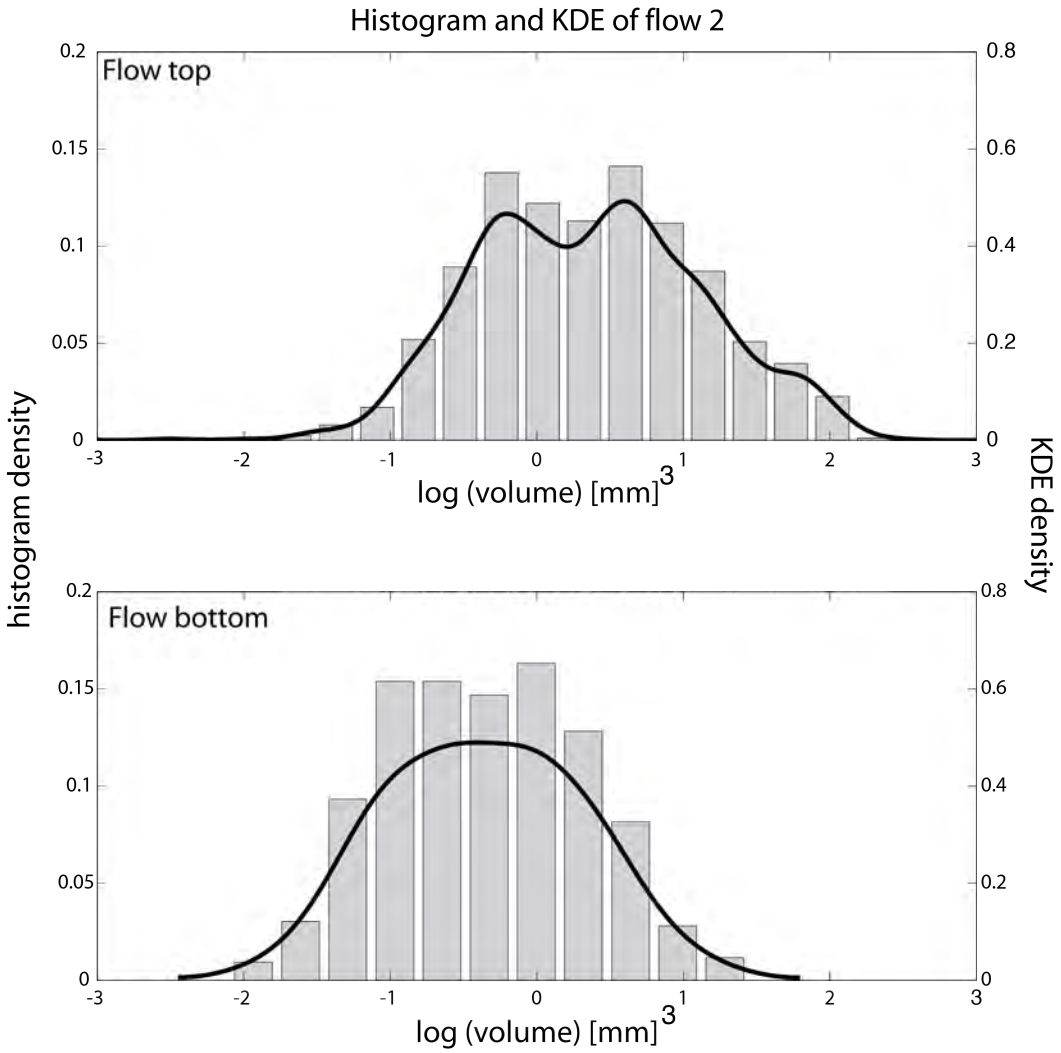

Figure S9. Flow 2: Histogram and Kernel Density Estimator of amygdale volumes from both the flow top (upper panel), and flow bottom (lower panel). Density describes the likelihood for a random variable to take a given value. The KDE is used to compute a mode for the distribution, and is determined without knowing *a priori* the parametric model of the distribution. In the top panel, the rightmost mode is used because the leftmost one yields unphysical negative pressures. Air pressure calculated using distribution modes is not the primary method used in this study – see text for details.

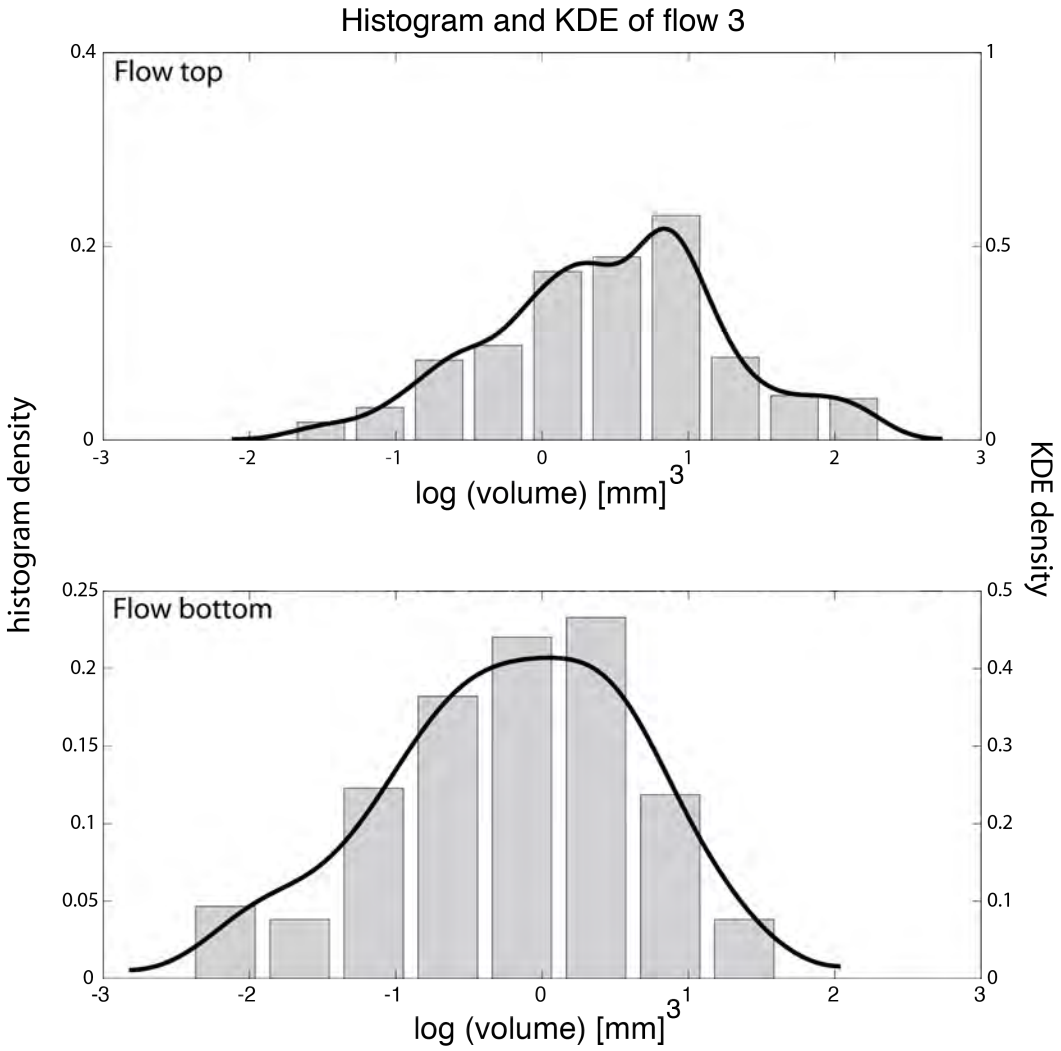

Figure S10. Flow 3: Histogram and Kernel Density Estimator (KDE) of amygdale volumes from both the flow top (upper panel), and flow bottom (lower panel). Density describes the likelihood for a random variable to take a given value. The KDE is used to compute a mode for the distribution, and is determined without knowing *a priori* the parametric model of the distribution. Air pressure calculated using distribution modes is not the primary method used in this study – see text for details.

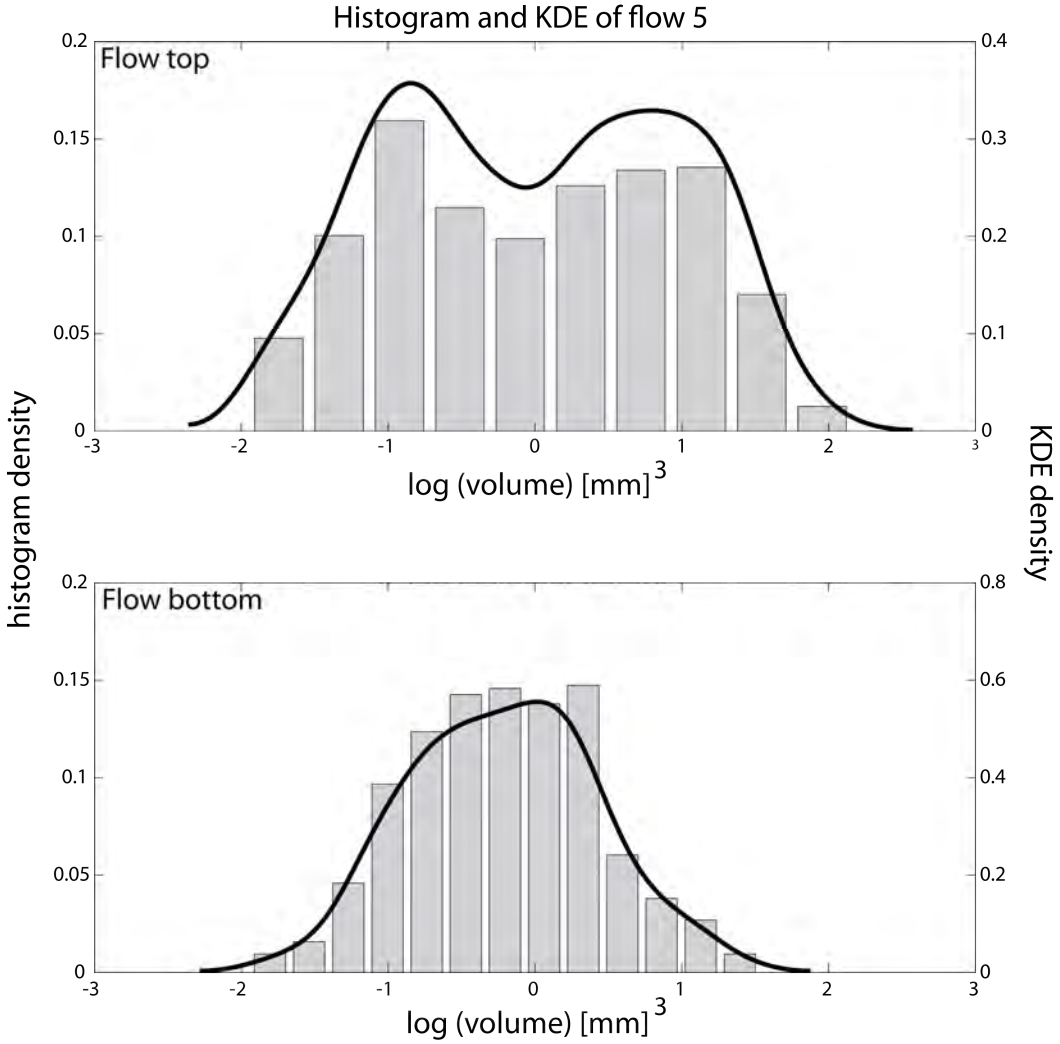

Figure S11. Flow 5: Histogram and Kernel Density Estimator of amygdale volumes from both the flow top (upper panel), and flow bottom (lower panel). Density describes the likelihood for a random variable to take a given value. The KDE is used to compute a mode for the distribution, and is determined without knowing *a priori* the parametric model of the distribution. In the top panel, the rightmost mode is used because the leftmost one yields unphysical negative pressures. Air pressure calculated using distribution modes is not the primary method used in this study – see text for details.

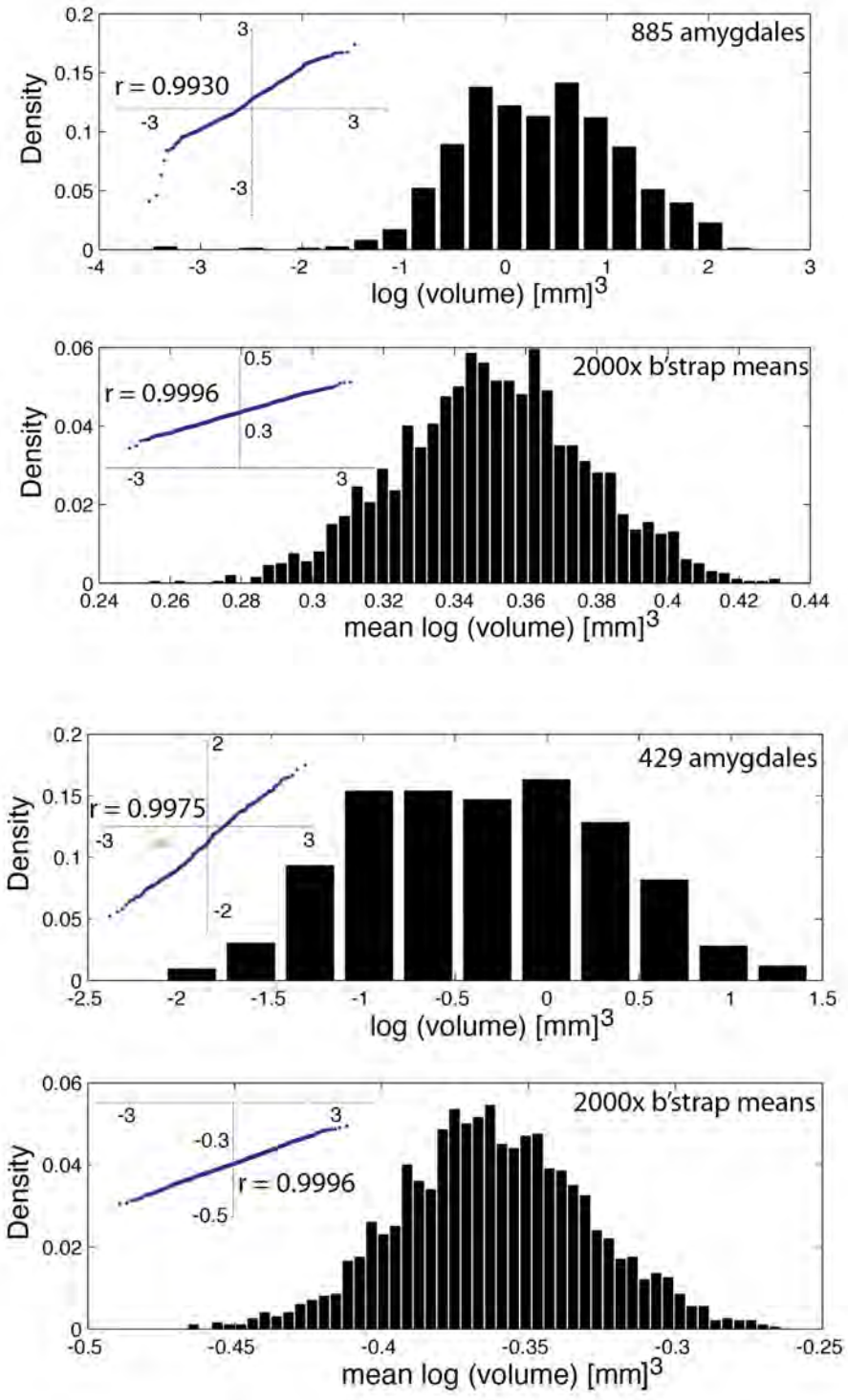

Figure S12: Amygdale volume size distribution resulting from X-ray analysis results of Flow 2. Density describes the likelihood for a random variable to take a given value. A) Flow Top (UVZ), B) Flow bottom (LVZ). Panels C) and D) represent bootstrap sampling distribution of the mean. The results from this flow give a pressure of 0.14 +/- 0.04 (2σ) bar. Normal quantile plots graph the z-score of the data in the x-axis (how many standard deviations a data point is from the mean), and y-axis identifies the amygdale log volume (or mean log volume for the boostrapped dataset). A correlation coefficient greater than 0.9976 is required to accept the null hypothesis that the data came from a normal distribution.

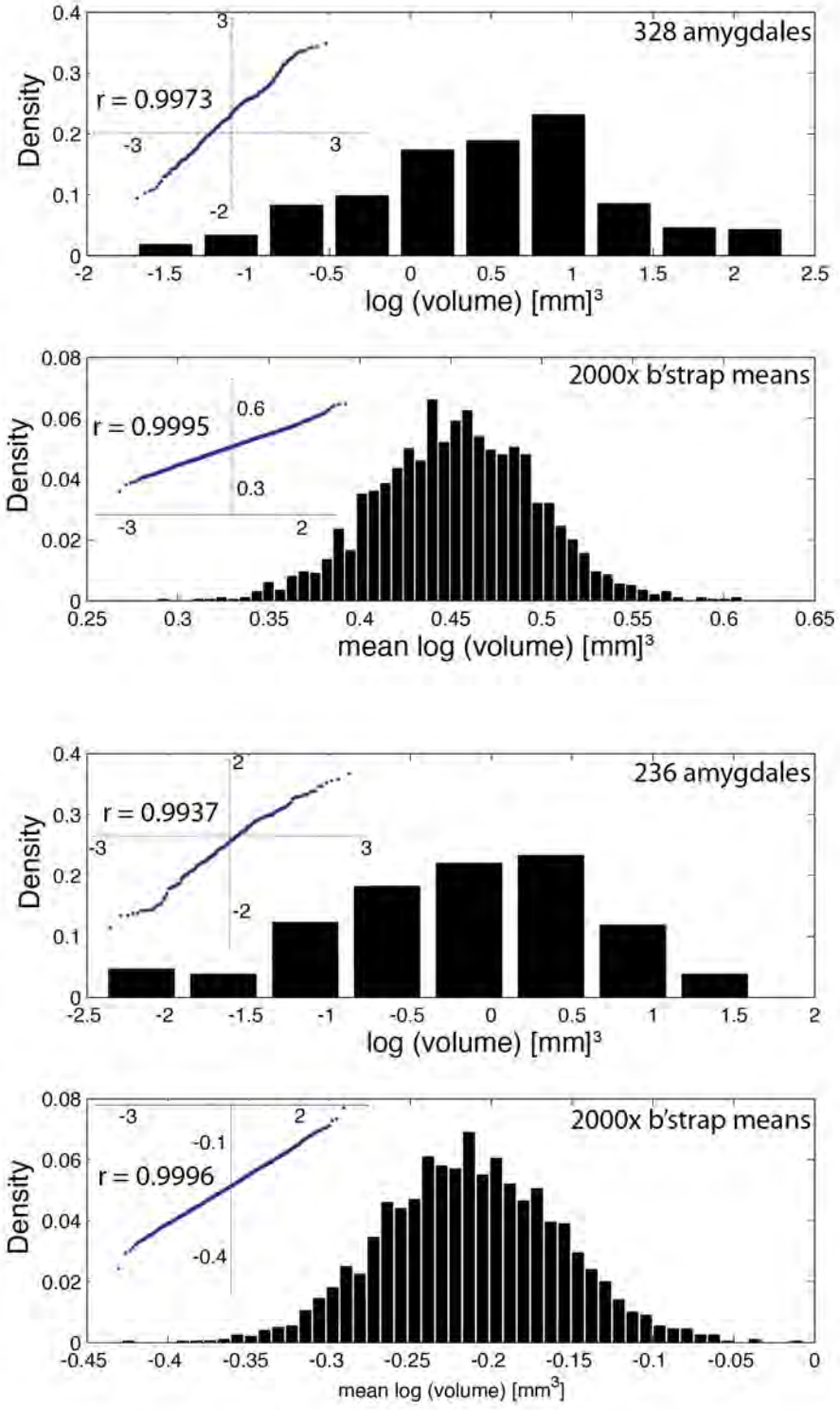

Figure S13: Amygdale volume size distribution resulting from X-ray analysis results of Flow 3. Density describes the likelihood for a random variable to take a given value. A) Flow Top (UVZ), B) Flow bottom (LVZ). Panels C) and D) represent the bootstrap sampling distribution of the mean. The results from this flow give a pressure of 0.11 +/- 0.05 (2σ) bar. Normal quantile plots graph the z-score of the data in the x-axis (how many standard deviations a data point is from the mean), and y-axis identifies the amygdale log volume (or mean log volume for the boostrapped dataset). A correlation coefficient greater than 0.9976 is required to accept the null hypothesis that the data came from a normal distribution.

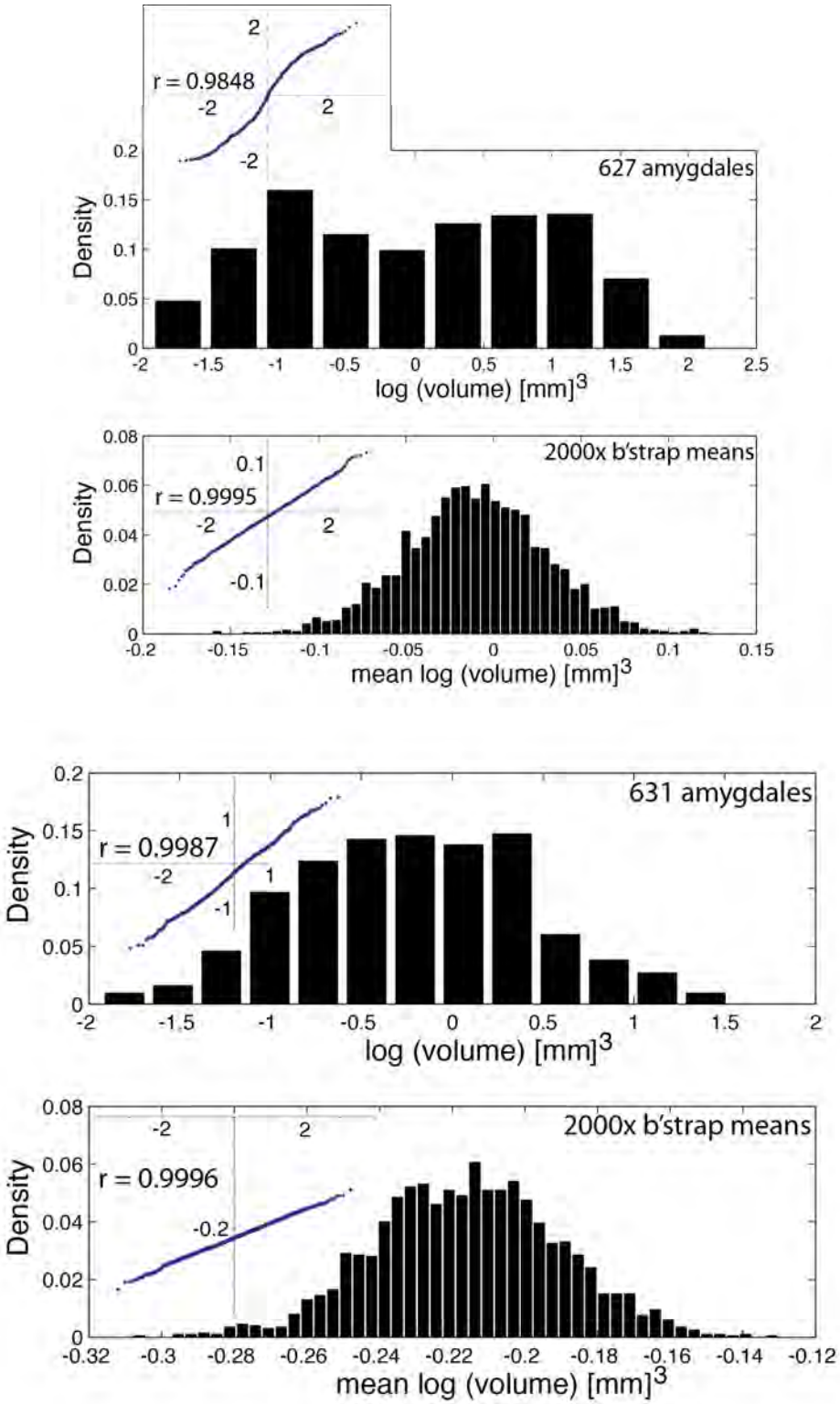

Figure S14: Amygdale volume size distribution resulting from X-ray analysis results of Flow 5. Density describes the likelihood for a random variable to take a given value. A) Flow Top (UVZ), B) Flow bottom (LVZ). Panels C) and D) represent the bootstrap sampling distribution of the mean. The results from this flow give a pressure of 0.40 +/- 0.23 (2σ) bar. Normal quantile plots graph the z-score of the data in the x-axis (how many standard deviations a data point is from the mean), and y-axis identifies the amygdale log volume (or mean log volume for the boostrapped dataset). A

correlation coefficient greater than 0.9976 is required to accept the null hypothesis that the data came from a normal distribution.